DES Y1 results: Splitting growth and geometry to test math xmlns="http://www.w3.org/1998/Math/MathML" display="inline">mi mathvariant="normal">Λ /mi>mi>CDM/mi>/math>

J. Muir et al. (DES Collaboration)

Phys. Rev. D **103**, 023528 — Published 21 January 2021

DOI: 10.1103/PhysRevD.103.023528

DES-2019-0520
FERMILAB-PUB-20-529-AE

DES Y1 results: Splitting growth and geometry to test ΛCDM

J. Muir,[1,*] E. Baxter,[2] V. Miranda,[3] C. Doux,[4] A. Ferté,[5] C. D. Leonard,[6] D. Huterer,[7] B. Jain,[4] P. Lemos,[8] M. Raveri,[9] S. Nadathur,[10] A. Campos,[11,12] A. Chen,[7] S. Dodelson,[11] J. Elvin-Poole,[13,14] S. Lee,[15] L. F. Secco,[4] M. A. Troxel,[15] N. Weaverdyck,[7] J. Zuntz,[16] D. Brout,[17,18] A. Choi,[13] M. Crocce,[19,20] T. M. Davis,[21] D. Gruen,[22,1,23] E. Krause,[3] C. Lidman,[24,25] N. MacCrann,[13,14] A. Möller,[26] J. Prat,[27] A. J. Ross,[13] M. Sako,[4] S. Samuroff,[11] C. Sánchez,[4] D. Scolnic,[15] B. Zhang,[25] T. M. C. Abbott,[28] M. Aguena,[29,30] S. Allam,[31] J. Annis,[31] S. Avila,[32] D. Bacon,[10] E. Bertin,[33,34] S. Bhargava,[35] S. L. Bridle,[36] D. Brooks,[8] D. L. Burke,[1,23] A. Carnero Rosell,[37,38] M. Carrasco Kind,[39,40] J. Carretero,[41] R. Cawthon,[42] M. Costanzi,[43,44] L. N. da Costa,[30,45] M. E. S. Pereira,[7] S. Desai,[46] H. T. Diehl,[31] J. P. Dietrich,[47] P. Doel,[8] J. Estrada,[31] S. Everett,[48] A. E. Evrard,[49,7] I. Ferrero,[50] B. Flaugher,[31] J. Frieman,[31,9] J. García-Bellido,[32] T. Giannantonio,[51,52] R. A. Gruendl,[39,40] J. Gschwend,[30,45] G. Gutierrez,[31] S. R. Hinton,[21] D. L. Hollowood,[48] K. Honscheid,[13,14] B. Hoyle,[47,53,54] D. J. James,[55] T. Jeltema,[48] K. Kuehn,[56,57] N. Kuropatkin,[31] O. Lahav,[8] M. Lima,[29,30] M. A. G. Maia,[30,45] F. Menanteau,[39,40] R. Miquel,[58,41] R. Morgan,[42] J. Myles,[22] A. Palmese,[31,9] F. Paz-Chinchón,[51,40] A. A. Plazas,[59] A. K. Romer,[35] A. Roodman,[1,23] E. Sanchez,[60] V. Scarpine,[31] S. Serrano,[19,20] I. Sevilla-Noarbe,[60] M. Smith,[61] E. Suchyta,[62] M. E. C. Swanson,[40] G. Tarle,[7] D. Thomas,[10] C. To,[22,1,23] D. L. Tucker,[31] T. N. Varga,[53,54] J. Weller,[53,54] and R.D. Wilkinson[35]

(DES Collaboration)

[1] *Kavli Institute for Particle Astrophysics & Cosmology, P. O. Box 2450, Stanford University, Stanford, CA 94305, USA*
[2] *Department of Physics and Astronomy, Watanabe 416, 2505 Correa Road, Honolulu, HI 96822*
[3] *Department of Astronomy/Steward Observatory, University of Arizona, 933 North Cherry Avenue, Tucson, AZ 85721-0065, USA*
[4] *Department of Physics and Astronomy, University of Pennsylvania, Philadelphia, PA 19104, USA*
[5] *Jet Propulsion Laboratory, California Institute of Technology, 4800 Oak Grove Dr., Pasadena, CA 91109, USA*
[6] *School of Mathematics, Statistics and Physics, Newcastle University, Newcastle upon Tyne, NE1 7RU, UK*
[7] *Department of Physics, University of Michigan, Ann Arbor, MI 48109, USA*
[8] *Department of Physics & Astronomy, University College London, Gower Street, London, WC1E 6BT, UK*
[9] *Kavli Institute for Cosmological Physics, University of Chicago, Chicago, IL 60637, USA*
[10] *Institute of Cosmology and Gravitation, University of Portsmouth, Portsmouth, PO1 3FX, UK*
[11] *Department of Physics, Carnegie Mellon University, Pittsburgh, Pennsylvania 15312, USA*
[12] *Instituto de Física Teórica, Universidade Estadual Paulista, São Paulo, Brazil*
[13] *Center for Cosmology and Astro-Particle Physics, The Ohio State University, Columbus, OH 43210, USA*
[14] *Department of Physics, The Ohio State University, Columbus, OH 43210, USA*
[15] *Department of Physics, Duke University Durham, NC 27708, USA*
[16] *Institute for Astronomy, University of Edinburgh, Edinburgh EH9 3HJ, UK*
[17] *Center for Astrophysics, Harvard & Smithsonian, 60 Garden Street, Cambridge, MA 02138, USA*
[18] *NASA Einstein Fellow*
[19] *Institut d'Estudis Espacials de Catalunya (IEEC), 08034 Barcelona, Spain*
[20] *Institute of Space Sciences (ICE, CSIC), Campus UAB, Carrer de Can Magrans, s/n, 08193 Barcelona, Spain*
[21] *School of Mathematics and Physics, University of Queensland, Brisbane, QLD 4072, Australia*
[22] *Department of Physics, Stanford University, 382 Via Pueblo Mall, Stanford, CA 94305, USA*
[23] *SLAC National Accelerator Laboratory, Menlo Park, CA 94025, USA*
[24] *Centre for Gravitational Astrophysics, College of Science, The Australian National University, ACT 2601, Australia*
[25] *The Research School of Astronomy and Astrophysics, Australian National University, ACT 2601, Australia*
[26] *Université Clermont Auvergne, CNRS/IN2P3, LPC, F-63000 Clermont-Ferrand, France*
[27] *Department of Astronomy and Astrophysics, University of Chicago, Chicago, IL 60637, USA*
[28] *Cerro Tololo Inter-American Observatory, NSF's National Optical-Infrared Astronomy Research Laboratory, Casilla 603, La Serena, Chile*
[29] *Departamento de Física Matemática, Instituto de Física, Universidade de São Paulo, CP 66318, São Paulo, SP, 05314-970, Brazil*
[30] *Laboratório Interinstitucional de e-Astronomia - LIneA, Rua Gal. José Cristino 77, Rio de Janeiro, RJ - 20921-400, Brazil*
[31] *Fermi National Accelerator Laboratory, P. O. Box 500, Batavia, IL 60510, USA*
[32] *Instituto de Fisica Teorica UAM/CSIC, Universidad Autonoma de Madrid, 28049 Madrid, Spain*

[33] CNRS, UMR 7095, Institut d'Astrophysique de Paris, F-75014, Paris, France
[34] Sorbonne Universités, UPMC Univ Paris 06, UMR 7095, Institut d'Astrophysique de Paris, F-75014, Paris, France
[35] Department of Physics and Astronomy, Pevensey Building, University of Sussex, Brighton, BN1 9QH, UK
[36] Jodrell Bank Center for Astrophysics, School of Physics and Astronomy, University of Manchester, Oxford Road, Manchester, M13 9PL, UK
[37] Instituto de Astrofisica de Canarias, E-38205 La Laguna, Tenerife, Spain
[38] Universidad de La Laguna, Dpto. Astrofísica, E-38206 La Laguna, Tenerife, Spain
[39] Department of Astronomy, University of Illinois at Urbana-Champaign, 1002 W. Green Street, Urbana, IL 61801, USA
[40] National Center for Supercomputing Applications, 1205 West Clark St., Urbana, IL 61801, USA
[41] Institut de Física d'Altes Energies (IFAE), The Barcelona Institute of Science and Technology, Campus UAB, 08193 Bellaterra (Barcelona) Spain
[42] Physics Department, 2320 Chamberlin Hall, University of Wisconsin-Madison, 1150 University Avenue Madison, WI 53706-1390
[43] INAF-Osservatorio Astronomico di Trieste, via G. B. Tiepolo 11, I-34143 Trieste, Italy
[44] Institute for Fundamental Physics of the Universe, Via Beirut 2, 34014 Trieste, Italy
[45] Observatório Nacional, Rua Gal. José Cristino 77, Rio de Janeiro, RJ - 20921-400, Brazil
[46] Department of Physics, IIT Hyderabad, Kandi, Telangana 502285, India
[47] Faculty of Physics, Ludwig-Maximilians-Universität, Scheinerstr. 1, 81679 Munich, Germany
[48] Santa Cruz Institute for Particle Physics, Santa Cruz, CA 95064, USA
[49] Department of Astronomy, University of Michigan, Ann Arbor, MI 48109, USA
[50] Institute of Theoretical Astrophysics, University of Oslo. P.O. Box 1029 Blindern, NO-0315 Oslo, Norway
[51] Institute of Astronomy, University of Cambridge, Madingley Road, Cambridge CB3 0HA, UK
[52] Kavli Institute for Cosmology, University of Cambridge, Madingley Road, Cambridge CB3 0HA, UK
[53] Max Planck Institute for Extraterrestrial Physics, Giessenbachstrasse, 85748 Garching, Germany
[54] Universitäts-Sternwarte, Fakultät für Physik, Ludwig-Maximilians Universität München, Scheinerstr. 1, 81679 München, Germany
[55] Center for Astrophysics | Harvard & Smithsonian, 60 Garden Street, Cambridge, MA 02138, USA
[56] Australian Astronomical Optics, Macquarie University, North Ryde, NSW 2113, Australia
[57] Lowell Observatory, 1400 Mars Hill Rd, Flagstaff, AZ 86001, USA
[58] Institució Catalana de Recerca i Estudis Avançats, E-08010 Barcelona, Spain
[59] Department of Astrophysical Sciences, Princeton University, Peyton Hall, Princeton, NJ 08544, USA
[60] Centro de Investigaciones Energéticas, Medioambientales y Tecnológicas (CIEMAT), Madrid, Spain
[61] School of Physics and Astronomy, University of Southampton, Southampton, SO17 1BJ, UK
[62] Computer Science and Mathematics Division, Oak Ridge National Laboratory, Oak Ridge, TN 37831

We analyze Dark Energy Survey (DES) data to constrain a cosmological model where a subset of parameters — focusing on Ω_m — are split into versions associated with structure growth (e.g. $\Omega_m^{\rm grow}$) and expansion history (e.g. $\Omega_m^{\rm geo}$). Once the parameters have been specified for the ΛCDM cosmological model, which includes general relativity as a theory of gravity, it uniquely predicts the evolution of both geometry (distances) and the growth of structure over cosmic time. Any inconsistency between measurements of geometry and growth could therefore indicate a breakdown of that model. Our growth-geometry split approach therefore serves as both a (largely) model-independent test for beyond-ΛCDM physics, and as a means to characterize how DES observables provide cosmological information. We analyze the same multi-probe DES data as Ref. [1]: DES Year 1 (Y1) galaxy clustering and weak lensing, which are sensitive to both growth and geometry, as well as Y1 BAO and Y3 supernovae, which probe geometry. We additionally include external geometric information from BOSS DR12 BAO and a compressed Planck 2015 likelihood, and external growth information from BOSS DR12 RSD. We find no significant disagreement with $\Omega_m^{\rm grow} = \Omega_m^{\rm geo}$. When DES and external data are analyzed separately, degeneracies with neutrino mass and intrinsic alignments limit our ability to measure $\Omega_m^{\rm grow}$, but combining DES with external data allows us to constrain both growth and geometric quantities. We also consider a parameterization where we split both Ω_m and w, but find that even our most constraining data combination is unable to separately constrain $\Omega_m^{\rm grow}$ and $w^{\rm grow}$. Relative to ΛCDM, splitting growth and geometry weakens bounds on σ_8 but does not alter constraints on h.

I. INTRODUCTION

One of the major goals of modern cosmology is to better understand the nature of the dark energy that drives the Universe's accelerating expansion. Though the simplest model for dark energy, a cosmological constant Λ, is

* Corresponding author: jlmuir@stanford.edu

in agreement with nearly all observations to date, there exist a number of viable alternative models which explain the observed acceleration by introducing new fields or by extending general relativity via some form of modified gravity [2, 3]. Because there is no single most favored theoretical alternative, observational studies of dark energy largely consist of searches for tensions with the predictions of a minimal cosmological model, ΛCDM, which consists of a cosmological constant description of dark energy (Λ), cold dark matter (CDM), and general relativity as the theory of gravity.

A tension that has attracted significant attention is one between constraints on the amplitude of matter density fluctuations σ_8 made by low redshift measurements, e.g. by the Dark Energy Survey (DES), and by Planck measurements of the Cosmic Microwave Background (CMB). This comparison is often phrased in terms of $S_8 \equiv \sigma_8 \sqrt{\Omega_m/0.3}$, the parameter combination most constrained by weak lensing analyses. Though the DES and Planck results are not in tension according to the statistical metrics used in the original DES Year 1 analysis [4] (note that this is a topic of some discussion [5]), the DES constraints prefer slightly lower σ_8 than those from Planck. This offset is in a direction consistent with other lensing results [6–14], and has been demonstrated to be independent [15] of the much-discussed tension between CMB and local SNe measurements of the Hubble constant H_0 [16–18]. In fact, of the numerous theoretical studies focused on alleviating the H_0 tension, most have found a joint resolution of the σ_8 and H_0 tensions challenging, as discussed in e.g. Refs. [19–22]. Independent CMB measurements from ACT and WMAP give σ_8 constraints consistent with those from Planck [23], while constraints based solely on reconstructed Planck CMB lensing maps are consistent with σ_8 constraints from both DES and measurements of CMB temperature and polarization [24, 25].

These tensions are interesting because mismatched constraints from low and high-redshift probes could indicate a need to extend our cosmological model beyond ΛCDM. Of course, it is also possible that these offsets could be caused by systematic errors or a statistical fluke. Given this, it is important to examine how different observables contribute to the σ_8 (and H_0) tension, as well as what classes of model extensions have the potential to alleviate them.

With this goal in mind, we perform a consistency test between geometric measurements of expansion history and measurements of the growth of large scale structure. The motivation for this test is similar to that of the early- vs. late-Universe (Planck vs. DES) comparison: we want to check for agreement between two classes of cosmological observables that have been split in a physically motivated way. More ambitiously, we can also view this analysis as a search for signs of beyond-ΛCDM physics. The growth-geometry split is motivated in particular by the fact that modified gravity models have been shown to generically break the consistency between expansion and structure growth expected in ΛCDM [26–30].

Our analysis focuses on data from the Dark Energy Survey (DES). DES is an imaging survey conducted between 2013-2019 which mapped galaxy positions and shapes over a 5000 deg^2 area and performed a supernovae survey in a smaller 27 deg^2 region. This large survey volume and access to multiple observables make DES a powerful tool for constraining both expansion history and structure growth. Constraints on cosmological parameters from the first year of DES data (Y1) have been published for the combined analysis of galaxy clustering and weak lensing [4, 31], for the baryonic acoustic oscillation (BAO) feature in the galaxy distribution [32], and for galaxy cluster abundance [33]. Additionally, cosmological results have been reported for the first three years (Y3) of supernovae data [34], as well as for the combined analysis of Y3 SNe with Y1 galaxy clustering, weak lensing, and BAO [1]. Analyses of DES Y3 clustering and lensing data are currently underway. The results presented in this paper are based on a multi-probe analysis like that of Ref. [1].

Because weak lensing and large scale structure probes like those measured by DES mix information from growth and geometry [28, 35–39], rather than purely comparing ΛCDM constraints from two datasets, we introduce new parameters to facilitate this comparison. As we explain in more detail in Sect. II, we define separate "growth" and "geometry" versions of a subset of cosmological parameters Θ: $\Theta^{\rm grow}$ and $\Theta^{\rm geo}$. By constraining growth and geometry parameters simultaneously, we can answer questions like

- Are DES constraints driven more by growth or geometric information?
- Are the data consistent with the predictions of ΛCDM— that is, with $\Theta^{\rm grow} = \Theta^{\rm geo}$?
- Is the DES preference for low σ_8 compared to Planck driven more by its sensitivity to background expansion (geometry) or by its measurement of the evolution of inhomogeneities (growth)?

Our analysis thus serves as both a model-independent search for new physics affecting structure growth and an approach to building a deeper understanding of how DES observables contribute cosmological information.

The closest predecessors to the present work are Refs. [40–42] which introduce similar growth-geometry consistency tests and apply them to data. These analyses have the same general idea and approach as the present analysis, but differ in several important aspects of how they implement the theoretical modeling of observables in their split parameterization. In a similar spirit, Ref. [43] explores growth-geometry consistency without introducing new parameters, using instead dataset comparisons in a search for discordance with ΛCDM. These approaches are complemented by other attempts at model independent tests of dark energy and modified gravity [44, 45], including analyses involving meta parameters analogous

to our split parameterization [46–48], as well as other parameterizations which allow structure growth to deviate from expectations set by general relativity. These include analyses that have constrained free amplitudes multiplying the growth rate $f\sigma_8$ [49], or the "growth index" parameter γ [27, 50]. The commonly studied $\Sigma - \mu$ model of modified gravity [31, 51–54] is also in this category. In fact, the analysis presented below can be viewed as analogous to a Σ-μ study like that in Refs. [55, 56], with Σ fixed to its GR value, though differences in our physical interpretation of the added parameters changes how we approach analysis choices related to nonlinear scales.

A. Plan of analysis

Our goal is to test the consistency between DES Year 1 constraints from expansion and those from measurements of the growth of large scale structure. We will do this using using three different combinations of data:

1. DES data alone (including DES galaxy clustering and weak lensing, BAO, and supernovae measurements) — henceforth, "DES-only" or just "DES";
2. As above, plus external data constraining geometry only from Planck 2015 and BOSS DR12 BAO measurements — henceforth, "DES+Ext-geo";
3. As above, plus external growth information from BOSS DR12 RSD measurements — henceforth, "DES+Ext-all".

Our main results will come from the combination of all of these datasets, but we will use the DES-only and DES+Ext-geo subsets to aid our interpretation of how different probes contribute information.[1]

The motivation for this growth-geometry split parameterization is to study the mechanism behind late-time acceleration, so we focus on splitting parameters associated with dark energy properties. Primarily, we will focus on the case where we split the matter density parameter Ω_m in flat ΛCDM, that is

$$\Omega_m \to \{\Omega_m^{\rm geo}, \Omega_m^{\rm grow}\} \qquad [\text{Split } \Omega_m].$$

As we discuss in more detail below, with some caveats, this split essentially means that $\Omega_m^{\rm geo}$ controls quantities like comoving and angular distances, while $\Omega_m^{\rm grow}$ controls quantities like the growth factor. Because we impose the relation $\Omega_m + \Omega_\Lambda = 1$, this means we also split Ω_Λ, and $\Omega_m^{\rm grow} \neq \Omega_m^{\rm geo}$ necessarily implies $\Omega_\Lambda^{\rm growth} \neq \Omega_\Lambda^{\rm geo}$.

[1] We do not include constraints from Planck 2018 [57], eBOSS DR14 [58–60], or eBOSS DR16 [61] because those likelihoods were not available when we set up this analysis. At the end of this paper, in Sect. VII E, we will briefly discuss how updating to use those datasets might influence our results.

We will additionally show limited wCDM results where we split both Ω_m and the dark energy equation of state, w, that is

$$\{\Omega_m, w\} \to \{\Omega_m^{\rm geo}, \Omega_m^{\rm grow}\, w^{\rm geo}, w^{\rm grow}\} \quad [\text{Split } \Omega_m,\, w].$$

Similarly to the split Ω_m case, $w^{\rm geo}$ enters into calculations of comoving distances, while $w^{\rm grow}$ is used to compute, e.g., the growth factor. We wish to calculate the posteriors for the split parameters given the aforementioned data, and in particular test their consistency (whether $\Theta^{\rm geo} = \Theta^{\rm grow}$) and identify any tensions.

For the split Ω_m model we will additionally examine how fitting in the extended growth-geometry split parameter space affects constraints on other parameters, with an eye towards understanding degeneracies between the split parameters and $\sum m_\nu$, σ_8, $h \equiv H_0/\left[100\ \mathrm{km\,s^{-1}\,Mpc^{-1}}\right]$, and $A_{\rm IA}$. This will allow us to build a deeper understanding of how the various datasets we consider provide growth and geometry information. It will also allow us to weigh in on whether non-standard cosmological structure growth could potentially alleviate tensions between late- and early-Universe measurements of σ_8 and h.

Unless otherwise noted, we use the same modeling and analysis choices as the DES Year 1 cosmology analyses described in Refs. [1, 31, 62]. In order to ensure that our results are robust against various modeling choices and priors, we will follow similar blinding and validation procedures to those used in Ref. [31]'s analyses of DES Y1 constraints on beyond-wCDM physics.

The paper is organized as follows. In Sect. II we describe how we model observables in our growth-geometry split parameterization, and in Sect. III we introduce the data used to measure those observables. Sect. IV discusses our analysis procedure, including the steps taken to protect our results from confirmation bias in Sect. IV A, and our approach to quantifying tensions and model comparison in Sect. IV B. We present our main results, which are constraints on the split parameters and their consistency with ΛCDM, in Sect. V. Sect. VI contains additional results characterizing how our growth-geometry split parameterization impacts constraints on other cosmological parameters, including σ_8. We conclude in Sect. VII. We discuss validation tests in detail in Appendices A-D, and in Appendix E we show plots of results supplementing those in the main body of the text.

II. MODELING GROWTH AND GEOMETRY

We consider several cosmological observables in our analysis: galaxy clustering and lensing, BAO, RSD, supernovae and the CMB power spectra. We model these observables in a way that explicitly separates information from geometry (i.e. expansion history) and growth. The separation of growth and geometry is immediately clear for some probes; supernovae, for instance, are purely geometric because they directly probe the luminosity

distance. For other probes, however, this split is not obvious, or even necessarily unique. Throughout, we endeavor to make physically motivated, self-consistent choices, and will note where past studies of growth and geometry differ. We emphasize that we are not developing a new physical model, but are rather developing a phenomenological split of ΛCDM.

Since one of our primary interests is in probing the physics associated with cosmic acceleration, we will use "growth" to describe the evolution of density perturbations in the late universe. Below, we describe our approach to modeling the observables we consider, and summarize this information in Table I.

Because structure growth depends primarily on the matter density via $\rho_m \propto h^2\Omega_m$ and we would like to decouple this from expansion-based constraints on h, for both our split parameterizations we additionally split the dimensionless Hubble parameter $h \equiv H_0/(100\,\mathrm{km\,s^{-1}\,Mpc^{-1}})$. In practice we fix $h^{\rm grow}$ to a fiducial value because it has almost no effect on growth observables: varying h across its full prior range results in fractional changes that are less than a percent for all observables considered. We demonstrate in Appendix D that altering this choice by either not splitting h or marginalizing over $h^{\rm grow}$ has little impact on our results.

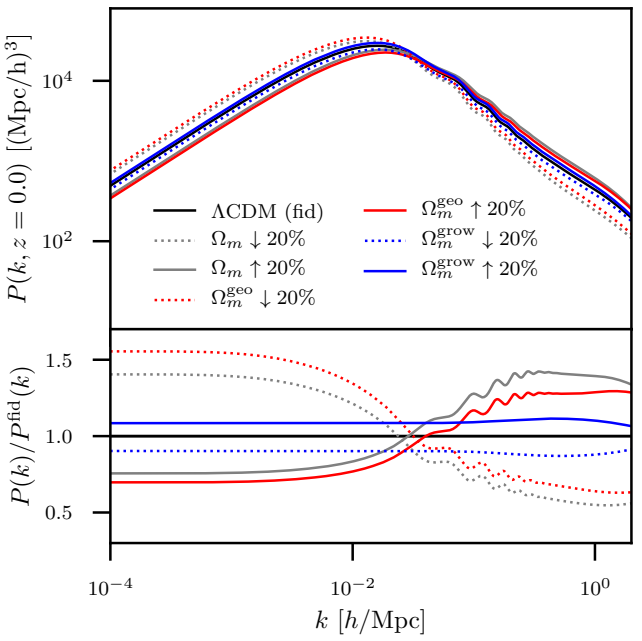

FIG. 1. Dependence of the nonlinear matter power spectrum on $\Omega_m^{\rm grow}$ and $\Omega_m^{\rm geo}$. Gray lines show the impact of changing Ω_m by ±20% in ΛCDM, red lines show changes to $\Omega_m^{\rm geo}$, and blue lines show changes to $\Omega_m^{\rm grow}$. The fiducial model uses $\Omega_m^{\rm grow} = \Omega_m^{\rm geo} = 0.295$. Solid lines correspond to an increase in the relevant Ω_m parameter to 0.354, while dotted lines show a decrease to 0.236.

A. Splitting the matter power spectrum

Several of the observables that we consider depend on the matter power spectrum, namely galaxy clustering and lensing, RSD, and the CMB power spectrum. The matter power spectrum $P(k, z)$ contains both growth and geometric information, so there is not a unique choice for how to compute it within our split parameterization. We choose a simple-to-implement and physically motivated approach. Because we use "growth" to describe the evolution of perturbations in the late universe, we assume that the early-time shape of the power spectrum is determined by geometric parameters.

More concretely, we construct the split linear power spectrum as a function of wavenumber k and redshift z, $P_{\rm lin}^{\rm split}(k, z)$, by combining linear matter power spectra computed separately using geometric or growth parameters:

$$P_{\rm lin}^{\rm split}(k, z) \equiv \frac{P_{\rm lin}^{\rm geo}(k, z_i)}{P_{\rm lin}^{\rm grow}(k, z_i)} P_{\rm lin}^{\rm grow}(k, z), \qquad (1)$$

where $P_{\rm lin}^{\rm geo}$ and $P_{\rm lin}^{\rm grow}$ are the linear matter power spectra computed in ΛCDM using the geometric and growth parameters, respectively, and z_i is an arbitrary redshift choice, to be discussed below. This definition has several desirable properties. First, if the growth and geometric parameters are the same, then it reduces to the standard ΛCDM linear power spectrum. Second, ignoring scale-dependent growth from neutrinos, $P_{\rm lin}^{\rm grow}(k, z)/P_{\rm lin}^{\rm grow}(k, z_i) = D^2(z)/D^2(z_i)$, where $D(z)$ is the linear growth factor. Consequently, the growth parameters will effectively control the growth of perturbations from z_i to z. Third, for $z \ll z_i$, this ratio of growth factors approaches one, so the early time matter power spectrum is controlled by the geometric parameters, as desired.

We compute nonlinear corrections to the matter power spectrum using HALOFIT [63–65]. HALOFIT provides a recipe, calibrated on simulations, for converting the linear matter power spectrum into the nonlinear power spectrum. As arguments to the HALOFIT fitting function, we use the mixed linear power spectrum from Eq. (1), and use the growth versions of the cosmological parameters. By using the growth parameters as arguments to HALOFIT, we ensure that nonlinear evolution is controlled by the growth parameters, and that if $\Theta^{\rm grow} = \Theta^{\rm geo}$, the resultant power spectrum agrees with that computed in the standard DES analyses of e.g., [4]. Although HALOFIT has not been explicitly validated for our growth-geometry split model, using it reasonable because we are performing a consistency test agaist ΛCDM rather than implementing a real physical model.

Fig. 1 shows how the full nonlinear power spectrum $P(k, z = 0)$ is affected by 20% changes to $\Omega_m^{\rm grow}$ (blue) and $\Omega_m^{\rm geo}$ (red). For comparison, we also show the effect of changes to Ω_m in ΛCDM (gray). The main effects of changing $\Omega_m^{\rm geo}$ are a scaling of the normalization of the

TABLE I. Modeling summary.

Observable	Modeling Ingredient	Described in	Geometry	Growth
Galaxy clustering and lensing	$P(k)$ shape at z_i	Sect. II A	✓	
	$P(k)$ evolution since z_i	Sect. II A		✓
	Projection to 2PCF	Sect. II B	✓	
	Intrinsic alignments	Sect. II B		✓
BAO	Distances	Sect. II C	✓	
RSD	$f(z)\sigma_8(z)/\sigma_8(0)$	Sect. II D		✓
	$\sigma_8(z=0)$	Sect. II D	✓	✓
Supernovae (SN)	Distances	Sect. II E	✓	
CMB	Compressed likelihood	Sect. II F	✓	

power spectrum and a change in the wavenumber where it peaks. This amplitude change occurs because the Poisson equation relates gravitational potential fluctuations Φ to matter density fluctuations δ via

$$k^2\,\Phi(k,z) = 4\pi G\rho_m\delta = \tfrac{3}{2}H_0^2\Omega_m(1+z)\,\delta(k,z). \quad (2)$$

Thus, for fixed primordial potential power spectrum, the matter power spectrum's early-time amplitude is proportional to $(\Omega_m^{\rm geo})^{-2}$. The peak of the power spectrum occurs at the wavenumber corresponding to the horizon scale at matter-radiation equality, $k_{\rm eq} \propto \Omega_m h^2$, so increasing $\Omega_m^{\rm geo}$ shifts the peak to higher k. Thus, the net effect of increasing $\Omega_m^{\rm geo}$ is a decrease in power at low k and an increase in power at high k. Changing $\Omega_m^{\rm grow}$, on the other hand, impacts the late time growth, leading to a roughly scale-independent change in the power spectrum. Nonlinear evolution at small scales breaks this scale-indepdence.

We use $z_i = 3.5$ as our fiducial value for the redshift at which growth parameters start controlling the evolution of the matter power spectrum. This choice is motivated by the fact that $z = 3.5$ is before the dark energy dominated era and is well beyond the redshift range probed by the DES samples. Raising z_i will slightly increase the sensitivity to growth because it means that the growth parameters control a greater portion of the history of structure growth between recombination and the present. However, as long as z_i is high enough, this has only a small effect on observables. For the values of $\Omega_m^{\rm grow}$ and $\Omega_m^{\rm geo}$ shown in Fig. 1, we confirm that increasing z_i to 5 or 10 results in changes of less than one percent at all wave numbers of $P_{\rm lin}^{\rm split}(k, z=0)$, and also at all angular scales of the DES galaxy clustering and weak lensing 2pt functions. Therefore, the combined constraints of DES and external data are weakly sensitive to the choice of z_i as we show in Appendix A.

B. Weak lensing and galaxy clustering

For a photometric survey like DES, galaxy and weak lensing correlations are typically measured via angular two-point correlation functions (2PCF). To make theory predictions for 2PCF we first compute the angular power spectra. Assuming flat geometry and using the Limber approximation [66, 67], the angular power spectrum between the ith redshift bin of tracer A and the jth redshift bin of tracer B is

$$C_{AB}^{ij}(\ell) = \int dz \frac{H(z)}{c\,\chi^2(z)} W_A^i(z) W_B^j(z) P(k,z)\Big|_{k=\left(\ell+\frac{1}{2}\right)/\chi(z)}. \quad (3)$$

Here χ is the comoving radial distance and $H(z)/(c\,\chi^2(z))$ is a volume element that translates three-dimensional density fluctuations into two-dimensional projected number density per redshift. The terms W_A^i and W_B^j are window functions relating fluctuations in tracers A and B to the underlying matter density fluctuations whose statistics are described by the power spectrum $P(k,z)$. The window functions for galaxy number density g and weak lensing convergence κ are, respectively

$$W_g^i(z,k) = n_i(z)\,b_i(z,k), \quad (4)$$

$$W_\kappa^i(z) = \left(\frac{3H_0^2\Omega_m}{2c^2}\right)\left(\frac{\chi(z)}{a(z)\,H(z)}\right) \times \int_z^\infty dz' n_i(z')\frac{\chi(z')-\chi(z)}{\chi(z')}. \quad (5)$$

In these expressions, $n_i(z)$ is the normalized redshift distribution of galaxies in sample i while $b_i(z,k)$ is their galaxy bias. Following the DES Y1 key-paper analysis [4], we will assume a constant linear bias for each sample, denoted with the parameter b_i.

In our growth-geometry split framework, we compute the power spectrum $P(k,z)$ in Eq. (3) via the procedure described in Sect. II A. We treat all projection operations in Eqs. (3)-(9) as geometric. This choice means that the usual σ_8-Ω_m weak lensing degeneracy will occur between between σ_8 (computed with $P_{\rm lin}^{\rm split}$) and $\Omega_m^{\rm geo}$, so we define $S_8 \equiv \sigma_8\sqrt{\Omega_m^{\rm geo}/0.3}$.

We include contributions to galaxy shear correlations from intrinsic alignments between galaxy shapes via a non-linear alignment model [68] which is the same intrinsic alignment model used in previous DES Y1 analyses [62]. This model adds a term to the shear convergence

window function,

$$W^i_\kappa(z) \to W^i_\kappa(z) - A_{\rm IA}\left[\left(\frac{1+z}{1+z_0}\right)^{\alpha_{IA}}\frac{C_1\rho_{m0}}{D(z)}\right] n_i(z). \tag{6}$$

Here $A_{\rm IA}$ and α_{IA} are free parameters which should be marginalized over when performing parameter inference. The normalization $C_1 = 0.0134/\rho_{\rm crit}$ is a constant calibrated based on SuperCOSMOS observations [68], ρ_{m0} is the present-day physical matter density, and $D(z)$ is the linear growth factor. Because intrinsic alignments are caused by cosmic structures, in our split formulation, we compute these quantities using growth parameters.

To obtain real-space angular correlation functions which can be compared to DES measurements, we then transform the angular power spectra of Eq. (3) using Legendre and Hankel transformations. The correlation between galaxy positions in tomographic bins i and j is

$$w^{ij}(\theta) = \sum_\ell \frac{2\ell+1}{4\pi} P_\ell(\cos\theta)\, C^{ij}_{gg}(\ell), \tag{7}$$

where $P_\ell(x)$ is Legendre polynomial of order ℓ. Shear correlations are computed in the flat-sky approximation as

$$\begin{aligned}\xi^{ij}_+(\theta) &= \int \frac{d\ell\,\ell}{2\pi} J_0(\ell\theta)\, C^{ij}_{\kappa\kappa}(\ell),\\ \xi^{ij}_-(\theta) &= \int \frac{d\ell\,\ell}{2\pi} J_4(\ell\theta)\, C^{ij}_{\kappa\kappa}(\ell).\end{aligned} \tag{8}$$

In these expressions, $J_m(x)$ is a Bessel function of the first kind of order m. Finally, the correlation between galaxy positions in bin i and tangential shears in bin j — the so-called "galaxy-galaxy lensing" signal — is similarly computed via

$$\gamma^{ij}_t(\theta) = \int \frac{d\ell\,\ell}{2\pi} J_2(\ell\theta)\, C^{ij}_{g\kappa}(\ell). \tag{9}$$

In our analysis, we perform these Fourier transformations using the function `tpstat_via_hankel` from the NICAEA software.[2] [69]

Several astrophysical and measurement systematics impact observed correlations for galaxy clustering and weak lensing. In addition to intrinsic alignments, which we addressed above, these include shear calibration and photometric redshift uncertainties. We model these effects following the previously published DES Y1 analyses [62], introducing several nuisance parameters that we marginalize over when performing parameter estimation. This includes a shear calibration parameters m_i for each redshift bin i where shear is measured and a photometric redshift bias parameter Δz_i for each redshift bin i. These systematic effects are not cosmology dependent and so are not impacted by the growth-geometry split.

[2] www.cosmostat.org/software/nicaea

C. BAO

Baryon acoustic oscillations (BAO) rely on a characteristic scale imprinted on galaxy clustering which is set by the sound horizon scale at the end of the Compton drag epoch. That characteristic physical sound horizon scale is

$$r_d = \int_{z_d}^\infty \frac{c_s(z)}{H(z)} dz, \tag{10}$$

where c_s is the speed of sound, z_d is the redshift of drag epoch, and $H(z)$ is the expansion rate at redshift z. Measurements of the BAO feature in galaxy clustering in directions transverse to the line of sight constrain $D_M(z)/r_d$, where $D_M(z) = (1+z)D_A(z)$ is the comoving angular diameter distance and $D_A(z)$ is the physical angular diameter distance. Line-of-sight measurements, on the other hand, constrain $H(z)r_d$. In practice constraints from BAO analyses are reported in terms of dimensionless ratios,

$$\alpha_\perp = \frac{D_M(z) r_d^{\rm fid}}{D_M^{\rm fid}(z) r_d} \tag{11}$$

and

$$\alpha_\parallel = \frac{H^{\rm fid}(z) r_d^{\rm fid}}{H(z) r_d}, \tag{12}$$

where the superscript "fid" indicates that the quantity is computed at a fiducial cosmology.

The cosmological information here comes fundamentally from measures of distances via the comparison between the observed scale of the BAO feature to the physical distance r_d. Given this, in our split parameterization we compute the expressions in Eqs. (11) and (12) using geometric parameters.

D. RSD

Redshift-space distortions (RSD) measure anisotropies in the apparent clustering of matter in redshift space. These distortions are caused by the infall of matter into overdensities, so the RSD allow us to measure the rate of growth of cosmic structure. RSD constraints are presented in terms of constraints on $f(z)\sigma_8(z)$, where $f(z) = d\ln D/d\ln a$ for linear density fluctuation amplitude D and scale factor $a = (1+z)^{-1}$. In our split parameterization, the amplitude $\sigma_8 \equiv \sigma_8(z=0)$ should match the value computed using the mixed power spectrum $P^{\rm split}_{\rm lin}$ from Eq. (1), while the time-evolution of $\sigma_8(z)/\sigma_8(0)$ and the growth rate $f(z)$ should be governed by growth parameters.

To achieve this, we proceed as follows. First, following the method used in Planck analyses [70] (see their Eq. 33), we use our growth parameters to compute

$$f(z)\sigma_8^{\rm grow}(z) = \frac{\left[\sigma_8^{(\delta v)}(z)\right]^2}{\sigma_8^{\rm grow}(z)}. \tag{13}$$

Here the superscript on $\sigma_8^{\rm grow}$ denotes that it was computed within ΛCDM using the growth parameters. The quantity $\sigma_8^{(\delta v)}$ is the smoothed density-velocity correlation; it is defined similarly to $\sigma_8(z)$, but instead of using the matter power spectrum $P(k,z)$ it is computed by integrating over the linear cross power between the matter density fluctuations δ and the divergence of the dark matter and baryon (but not neutrino) peculiar velocity fields in Newtonian-gauge, $v = -\nabla \mathbf{v}_N / H$. Ref. [70] motivates this definition by noting that it is close to what is actually being probed by RSD measurements.

In order to make σ_8 consistent with our split matter power spectrum definition from Eq. (1), we multiply Eq. (13) by the $z = 0$ ratio of σ_8, computed from $P_{\rm lin}^{\rm split}$, and $\sigma_8^{\rm grow}$. The quantity that we use to compare theory with RSD measurements is therefore:

$$f(z)\sigma_8(z) = f(z)\sigma_8^{\rm grow}(z) \times \frac{\sigma_8(0)}{\sigma_8^{\rm grow}(0)}. \tag{14}$$

This expression will be consistent with our method of defining the linear power spectrum in Eq. (1) as long as it is evaluated at $z < z_i$.

E. Supernovae

Cosmological information from supernovae comes from measurements of the apparent magnitude of Type Ia supernovae as a function of redshift. Because the absolute luminosity of Type Ia supernovae can be calibrated to serve as standard candles, the observed flux can be used as a distance measure. Even when the value of that absolute luminosity is not calibrated with more local distance measurements, the relationship between observed supernova fluxes and redshifts contains information about how the expansion rate of the universe has changed over time.

Measurements and model predictions for supernovae are compared in terms of the distance modulus μ, which is related to the luminosity distance d_L via

$$\mu = 5 \log \left[d_L / 10{\rm pc} \right]. \tag{15}$$

The observed distance modulus is nominally given by the sum of the apparent magnitude, m_B, and a term accounting for the combination of the absolute magnitude and the Hubble constant, M_0.

We follow the approach to computing this used in the DES Y3 supernovae analysis [71], also described in Ref. [72], and use the CosmoSIS module associated with the latter paper to perform the calculations. In practice, computing the distance requires a few additional modeling components. These include the width x_1 and color $\mathcal{C}$ of the light-curve, which are used to standardize the luminosity of the type Ia supernovae, as well as a parameter $G_{\rm host}$ which introduces a step function to account for correlations between supernovae luminosity and host galaxy stellar mass $M_{\rm host}$ ($G_{\rm host}$ is $+1/2$ if $M_{\rm host} > 10^{10} M_\odot$, $-1/2$ if $M_{\rm host} < 10^{10} M_\odot$). The final expression for the distance modulus in terms of these parameters is

$$\mu = m_B + \alpha x_1 - \beta \mathcal{C} + M_0 + \gamma G_{\rm host} + \Delta\mu_{bias}. \tag{16}$$

Here the calibration parameters α, β, and γ are fit to data using the formalism from Ref. [73], and the selection bias $\Delta\mu_{\rm bias}$ is calibrated using simulations [74]. The parameter M_0 is marginalized over during parameter estimation.

The cosmological information in supernovae observations comes from distance measurements, so in our split parameterization we compute these quantities using geometric parameters.

F. CMB

The cosmic microwave background (CMB) anisotropies in temperature and polarization are a rich cosmological observable with information about both growth and geometry. The geometric information primarily consists of the distance to the last scattering surface and the sound horizon size at recombination. Two parameters encapsulate how these distances (and through them, the cosmological parameters) impact the observed CMB power spectra: the shift parameter [75],

$$R_{\rm shift} \equiv \sqrt{\Omega_m (100h)^2} D_M(z_*)/c, \tag{17}$$

which describes the location of the first power spectrum peak, and the angular scale of the sound horizon at last scattering $\ell_A = \pi/\theta_*$,

$$\ell_A \equiv \pi D_M(z_*)/r_s(z_*). \tag{18}$$

Here z_* is the redshift of recombination, D_M is the comoving angular diameter distance at that redshift, and r_s is the comoving sound horizon size. In our split parameterization, we use geometric parameters to compute these quantities.

The CMB is sensitive to late-time structure growth in a few different ways. The ISW effect adds TT power at low-ℓ in a way that depends on the linear growth rate, and weak lensing from low-z structure smooths the peaks of the CMB power spectra at high-ℓ. To be self-consistent, the calculation of these effects should use the split power spectrum described in Sect. II A. Adapting the ISW and CMB lensing predictions to our split parameterization would therefore require a modification of the CAMB software[3] [76, 77] we use to compute power spectra. In order to simplify our analysis, we focus on a subset of measurements from the CMB that are closely tied to geometric observables, independent of late-time growth.

[3] http://camb.info

We do this via a compressed likelihood which describes CMB constraints on $R_{\rm shift}$, ℓ_A, $\Omega_b h^2$, n_s, and $A_{\rm s}$ after marginalizing over all other parameters, including $\sum m_\nu$ and $A_{\rm Lens}$. This approach is inspired by the fact that the CMB mainly probes expansion history, and thus dark energy, via the geometric information provided by the locations of its acoustic peaks [78], and by the compressed Planck likelihood provided in Ref. [53]; see Sect. III B 2 below for details. In this formulation, we have constructed our CMB observables to be independent of late-time growth, so we compute the model predictions for them with geometric parameters.

G. Modeling summary and comparison to previous work

Table I summarizes the sensitivity of the probes discussed above to growth and geometry. Briefly, we derive constraints from structure growth from the LSS observables — galaxy clustering, galaxy-galaxy lensing, weak lensing shear, and RSD — while all probes we consider provide some information about geometry. Constraints from BAO, supernovae, and the scale of the first peaks of the CMB provide purely geometric information. The LSS observables mix growth and geometry via their dependence on the power spectrum: its shape is set by geometry, while its evolution since $z_i = 3.5$ is governed by growth parameters. All projection translating from three-dimensional matter power to two-dimensional observed correlations are geometry dependent.

[NEW TEXT BEGINS HERE]

We now compare our choices to previous work.

For the CMB, our geometry-growth split choices are motivated by simple implementation and (since our focus is on DES data) the ease of interpretation. In this we roughly follow the approach in Ref. [41] who also consider a compressed CMB likelihood that is governed purely by geometry. In contrast, Ref. [40] describes CMB fluctuations (and so the sound horizon scale) using growth parameters, then uses geometry parameters in converting physical to angular scales. Ref. [42] splits the growth and geometric information in the CMB by multipole, using the TT, TE, and EE power spectra at $\ell > 30$ to constrain geometric parameters, and the low ℓ (<30) multipoles as well as the lensing power spectrum to constrain growth.

For weak lensing, our approach is closest to Ref. [41], with an additional modification in how we model the matter power spectrum, described in Sec. II A. Ref. [42] leaves weak lensing out of their analysis, citing the difficulty in separating growth and geometric contributions to those observables. Both Refs. [40] and [41] compute the matter power spectrum entirely using growth parameters (as opposed to our split parameterization described in Sec. II A) and (like us) they use geometric prarameters for projection operations and for the distances used to computing the weak lensing kernel. These analyses differ in how they treat the lensing kernel's Ω_M^2 prefactor (see Eq. (5)). Ref. [40] treats this as a growth quantity, while Ref. [41] considers it part of the lensing window function and hence a geometric quantity. Our choice, which matches that of Ref. [41], means $\Omega_m^{\rm grow}$ affects weak lensing observables solely through changes in the matter power spectrum. Though this weakens our ability to constrain $\Omega_m^{\rm grow}$, it has the benefit of making our model more phenomenologically similar to other parameterizations of non-standard structure growth, making the interpretation of results more easily generalizable.

Our treatment of BAO and Type Ia Supernovae agrees with all previous literature in treating these probes as purely geometrical. Finally, our treatment of the RSD is subtly different from previous literature on the subject [40–42] who assumed $f\sigma_8$ are determined purely by the growth parameters, Our RSD is *mostly* determined by the growth of structure, but we allow $\sigma_8(z = 0)$ to also include geometric parameters via our split parameterization of the matter power spectrum.

[NEW TEXT ENDS HERE]

III. DATA AND LIKELIHOODS

In this section we describe the data and likelihoods used for our analyses. The datasets and where to find their descriptions are summarized in Table II.

A. DES Year 1 combined data

In our growth-geometry split analysis of DES data, we perform a combined analysis of DES Y1 galaxy clustering and weak lensing, DES Y1 BAO, and DES Y3 supernovae measurements, following a similar methodology to the multi-probe analysis in Ref. [1]. The combination of these measurements will be referred to as "DES" in the reported constraints below. We now describe the constituent measurements.

Galaxy samples used in these measurements were constructed from the DES Y1 Gold catalog [79], which is derived from imaging data taken between August 2013 and February 2014 using the 570-megapixel Dark Energy Camera [80] at CTIO. The data in the catalog covers an area of 1321 deg^2 in grizY filters and was processed with the DES Data Management system [81–84].

1. *DES Y1 Galaxy clustering and weak lensing*

The DES Y1 combined galaxy clustering and weak lensing analysis, hereafter Y1-3×2pt, is based on the analysis of three types of angular two-point correlation functions (2PCF): the correlation between the positions of a population of lens galaxies, between the measured shapes of a population of source galaxies, and the correlation of lens positions and source shapes. The lens

TABLE II. Table summarizing datasets included and abbreviations for plots.

Combination	Datasets	Described in	Geometry	Growth
DES	DES Y1 3 × 2pt (galaxy clustering and WL)	Sect. III A 1	✓	✓
	DES Y1 BAO	Sect. III A 2	✓	
	DES Y3 + lowZ SNe	Sect. III A 3	✓	
Ext-geo	Compressed 2015 Planck likelihood	Sect. III B 2	✓	
	BOSS DR12 BAO	Sect. III B 1	✓	
Ext-all	Ext-geo		✓	
	BOSS DR12 RSD	Sect. III C	✓	✓

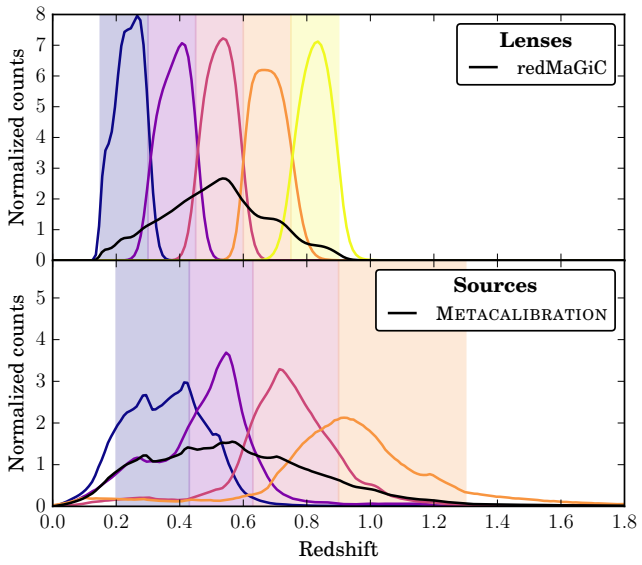

FIG. 2. Redshift distribution of source and lens galaxies used in the DES Y1-3×2pt analysis. The vertical shaded bands represent the nominal range of the redshift bins, while the solid lines show their estimated true redshift distributions, given their photometric-redshift-based selection.

galaxy sample consists of approximately 660,000 luminous red galaxies which were found using the REDMAGIC algorithm [85] and were selected using luminosity cuts to have relatively small photo-z errors. They are split into five redshift bins with nominal edges at $z = \{0.15, 0.3, 0.45, 0.6, 0.75, 0.9\}$. Weak lensing shears are measured from the source galaxy sample, which includes 26 million galaxies. These were selected from the Y1 Gold catalog using the METACALIBRATION [86, 87] and NGMIX[4] algorithms, and the BPZ algorithm [88] is used to estimate redshifts. The source galaxies are split into four redshift bins with approximately equal densities, with nominal edges at $z = \{0.2, 0.43, 0.63, 0.9, 1.3\}$ [89, 90]. For each source bin a multiplicative shear calibration parameter m_i for $i \in \{1, 2, 3, 4\}$ is introduced in order to prevent shear measurement noise and selection effects from biasing cosmological results. METACALIBRATION provides tight Gaussian priors on these parameters. The redshift distributions for the lens and source galaxies used in the DES Y1 galaxy clustering and weak lensing measurements are shown in Fig. 2. Uncertainties in photometric redshifts are quantified with nine nuisance parameters Δz_i^x which quantify translations of each redshift bin's distribution to $n_i^x(z - \Delta z_i^x)$, where i labels the redshift bin and x = source or lens.

The 2PCF measurements that comprise the Y1-3×2pt data are presented in Ref. [91] (galaxy-galaxy), Ref. [92] (galaxy-shear), and Ref. [93] (shear-shear). Each 2PCF is measured in 20 logarithmic bins of angular separation from 2.5′ to 250′ using the TREECORR [94] algorithm. Angular scale cuts are chosen as described in Ref. [62] in order to remove measurements at small angular scales where our model is not expected to accurately describe the impact of nonlinear evolution of the matter power spectrum and baryonic feedback. The resulting DES Y1-3×2pt data vector contains 457 measured 2PCF values. The likelihood for the 3 × 2pt analysis is assumed to be Gaussian in that data vector. The covariance is computed using COSMOLIKE [95], which employs a halo-model-based calculation of four-point functions [96]. Refs. [95, 97] present more information about the calculation and validation of the covariance matrix.

2. *DES Y1 BAO*

The measurement of the signature of baryon acoustic oscillations (BAO) in DES Y1 data is presented in Ref. [32]. That measurement is summarized as a likelihood of the ratio between the angular diameter distance and the drag scale $D_A(z = 0.81)/r_d$. This result was derived from the analysis of a sample of 1.3 million galaxies from the DES Y1 Gold catalog known as the DES BAO sample. These galaxies in the sample have photometric redshifts between 0.6 and 1.0 and were selected using color and magnitude cuts in order to optimize the high redshift BAO measurement, as is described in Ref. [98]. An ensemble of 1800 simulations [99] and three different methods for measuring galaxy clustering [100–102] were used to produce the DES BAO likelihood.

The DES BAO sample is measured from the same survey footprint as the samples used in the DES Y1-3×2pt

[4] https://github.com/esheldon/ngmix

analysis, so there will be some correlation between the two measurements. Following Ref. [1], we neglect this correlation when combining the two likelihoods. This can be motivated by the fact that the intersection between the 3×2pt and BAO galaxy samples is estimated to be about 14% of the total BAO sample, and the fact that no significant BAO signal is measured in the 2PCF measured for the 3×2pt analysis.

3. *DES Y3 + lowZ Supernovae*

The cosmological analysis of supernovae magnitudes from the first three years of DES observations is presented in Ref. [34]. The 207 supernovae used in this analysis were discovered via repeated deep-field observations of in a 27 deg^2 region of the sky taken between August 2013 and February 2016, and are in the redshift range $0.07 < z < 0.85$. A series of papers describe the search and discovery [84, 103, 104], calibration [105, 106], photometry [107], spectroscopic follow-up [108], simulations [109], selection effects [110], and analysis methodology [71] that went into those results. Following the DES supernovae analysis [1, 34] (but not the fiducial choices of the multi-probe analysis of Ref. [1]), we additionally include in the supernovae sample the so-called low-z subset: 122 supernovae at $z < 0.1$ that were measured as part of the Harvard-Smithsonian Center for Astrophysics Surveys [111, 112] and the Carnegie Supernova Project [113].

The DES supernovae likelihood is a Multivariate Gaussian in the difference between the predicted and measured values of the distance modulus μ. The likelihood is implemented in our analysis pipeline using the CosmoSIS Pantheon [72] module, adapted to use the DES measurements instead of the original Pantheon supernovae sample.

B. External geometric data

1. *BOSS DR12 BAO*

We use BAO information from the constraints presented in the BOSS Data Release 12 [49]. The likelihood provided by BOSS has a default fiducial r_d, and measurements on $D_M(z)$ and $H(z)$ (described in Sect. II C) at the redshifts $z = \{0.38, 0.51, 0.61\}$. These constraints include measurements of the Hubble parameter $H(z)$ and comoving angular diameter distance $d_A(z)$ at redshifts $z = \{0.38, 0.51, 0.61\}$. Specifically, we use the post-reconstruction BAO-only consensus measurements data file `BAO_consensus_results_dM_Hz.txt` and covariance files `BAO_consensus_covtot_dM_Hz.txt` provided on the BOSS results page.[5] No covariance with other data is assumed.

[5] https://www.sdss3.org/science/boss_publications.php

2. *Compressed Planck likelihood*

In order to extract information from Planck data that is independent of our growth parameters, we make our own version of the compressed Planck likelihood presented in Ref. [53]. This likelihood is a five-dimensional Gaussian likelihood extracted from a Multinest chain run with the Planck lite 2015 likelihood using the temperature power spectrum (TT) and low-ℓ temperature and polarization, with no lensing. We ran this chain using the same settings as used for the Planck constraints reported in the DES Y1 papers [4], which includes fixing $w = -1$ and marginalizing over neutrino mass. We also marginalize over the lensing amplitude $A_{\rm Lens}$ to reduce the possible impact of growth via weak lensing on the temperature power spectrum. From that chain we extracted a 5D mean and covariance for the parameter vector $[R_{\rm shift}, \ell_A, \Omega_b h^2, n_s, 10^9 A_{\rm s}]$. The compressed likelihood is then a five-dimensional multivariate Gaussian in those parameters. We confirm that this compressed likelihood is an accurate representation of the Planck constraints in this five-dimensional parameter space — in other words, that the Planck likelihood is approximately Gaussian — by checking that the chain samples for the full Planck likelihood follow a χ^2 distribution when evaluated relative to the mean and covariance used in the compressed likelihood.

C. External growth data (RSD)

We include an external growth probe using the BOSS DR12 combined results [49]. We use the full-power-spectrum-shape-based consensus measurements data file `final_consensus_results_dM_Hz_fsig.tx` and covariance file `final_consensus_covtot_dM_Hz_fsig.txt` provided on the BOSS results page.[5] This includes consensus measurements of $D_M(z)$, $H(z)$, and $f(z)\sigma_8(z)$ at the same three redshifts $z = \{0.38, 0.51, 0.61\}$ as the BAO-only likelihood. The reported values are the combined results from seven different measurements using different techniques and modeling assumptions, where the covariances between those results have been assessed using mock catalogues [114, 115].

As a slight complication, we note that these BOSS results use both the post-reconstruction BAO-only fits described in Sect. III B 1, and those from the full-shape analysis of the pre-reconstruction data. The combination of the post-reconstruction BAO and pre-reconstruction full-shape fits tightens constraints on $D_M(z)$ by around 10% and on $H(z)$ by 15-20%. This means that in addition to adding growth information from RSD, our Ext-all data combination will also have slightly tighter geometric constraints than Ext-geo.

IV. ANALYSIS CHOICES AND PROCEDURE

We use the same parameters and parameter priors as previous DES Y1 analyses [1, 4, 31]. For our split parameters, we use the same prior as their unsplit counterparts' priors in those previous analyses:

$$\Omega_m,\ \Omega_m^{\rm geo},\ \Omega_m^{\rm grow} \in [0.1, 0.9] \quad (19)$$
$$w,\ w^{\rm geo},\ w^{\rm grow} \in [-2.0, 0.33] \quad (20)$$

We use the same angular scale cuts for the DES Y1 weak lensing and LSS measurements, leaving 457 data points in the weak lensing and galaxy clustering combined 3×2pt data vector. The DES BAO likelihood contributes another measurement (of $D_A(z=0.81)/r_d$), and the DES SNe likelihood is based on measurements of 329 supernovae (207 from DES, 122 from the low-z sample). This means that our DES-only analysis is based on a total of 787 data points. The DES+Ext-geo analysis therefore has 798 data points (787 from DES, 5 from compressed Planck, 6 from BOSS BAO), and the DES+Ext-all analysis has 801 (same as DES+Ext-geo plus 3 BOSS RSD measurements).

Calculations were done in the CosmoSIS[6] software package [116], using the same pipeline as the Y1KP, modulo changes to implement the growth-geometry split. For validation tests, chains were run with Multinest sampler [117–119], with low resolution fast settings of 250 live points, efficiency 0.3, and tolerance 0.01. For fits to data where we need both posteriors and Bayesian evidence, we use Polychord [120] with 250 live points, 30 repeats, and tolerance of 0.01. Summary statistics and contour plots from chains are done using the GetDist [121] software with a smoothing kernel of 0.5.

As noted in Sect. I A, our main results will be products of parameter estimation and model comparison evaluated for

- Split Ω_m constrained with DES+Ext-geo, and
- Split Ω_m constrained with DES+Ext-all.

This choice was based on simulated analyses performed before running parameter estimation on real data. In these analyses we computed model predictions for observables at a fiducial cosmology, then analyzed those predictions as if they were measurements. By studying the relationship between the resulting posteriors and the input parameter values we identified which model-data combinations are constraining enough so that parameter estimates are unbiased by parameter-space projection effects. This is described in more detail in Appendix B. For the DES+Ext-geo and DES+Ext-all constraints on split Ω_m, we confirm that the input parameter values are contained within the 68% confidence intervals of the synthetic-data versions of all marginalized posteriors plotted in this paper.

We consider two additional sets of constraints:

- Split Ω_m constrained by DES only, and
- Split Ω_m and w constrained by DES+Ext-all.

Our simulated analyses revealed that the one-dimensional marginalized posteriors are impacted by significant projection effects. Given this, for these cases we not report numerical parameter estimates or error bars, but we will still report model comparison statistics (to be discussed in Sect. IV B) and show their two-dimensional confidence regions on plots. We do not consider constraints splitting both Ω_m and w for DES-only and DES+Ext-geo because these datasets are less constraining than DES+Ext-all and so are expected to suffer from even more severe projection effects. A more detailed discussion of these projection effects and the parameter degeneracies which cause them can be found in Appendix B.

We follow a procedure similar to that used in Ref. [31] to validate our analysis pipeline. Our goal is to characterize the robustness of our results to reasonable changes to analysis choices, as well as to astrophysical or modeling systematics. The analysis presented in this paper was blinded in the sense that all analysis choices were fixed and we ensured that the pipeline passed a number of predetermined validation tests before we looked at the true cosmological results. The blinding procedure and these tests are described below.

A. Validation

In planning and executing this study, we took several steps to protect the results against possible experimenter bias, following a procedure similar to the parameter-level blinding strategy used in previous DES Y1 beyond-ΛCDM analyses. Key to this were extensive simulated analyses, in which we analyzed model predictions for observables with known input parameters as if they were data. All analysis choices are based on these simulated analyses, including which datasets we focus on and how we report results. Before running our analysis pipeline on real data, we wrote the bulk of this paper's text, including the plan of how the analysis would proceed, and subjected that text to a preliminary stage of DES internal review.

When performing parameter estimation on the real data, we concealed the cosmology results using the following strategies:

- We avoided over-plotting measured data and theory predictions for observables.
- We post-processed all chains so that the mean of the posterior distributions lay on our fiducial cosmology.

[6] https://bitbucket.org/joezuntz/cosmosis/

- We do not look at model comparison measures between our split parameterization and ΛCDM.

We maintained these restrictions until we confirmed that the analysis passed several sets of validation tests:

- We confirm that our results cannot be significantly biased by any one of the sample systematics adopted in our validation tests. To do this we check that the parameter estimates we report change by less than 0.3σ when we contaminate synthetic input data with a number of different effects, including non-linear galaxy bias and a more sophisticated intrinsic alignment model. This test is discussed Appendix C.

- We confirm that non-offset ΛCDM chains give results consistent with what Ref. [1] reports.[7]

- We studied whether our main results are robust to changes in our analysis pipeline. We found that parameter constraints shift by less than 0.3σ when we apply more aggressive cuts to removing non-linear angular scales, and when we use an alternative set of photometric redshifts.

  Our results did change when we replaced the intrinsic alignment model defined Eq. (6) with one where the amplitude $A_{\rm IA}$ varies independently in each source redshift bin. Upon further investigation, detailed in Appendix D, we found that a similar posterior shift manifests in the analysis of synthetic data, so we believe that it is due to a parameter-space projection effect rather than a property of the real DES data. We therefore proceed with the planned analysis despite failing this robustness test, but add an examination of how intrinsic alignment properties covary with our split parameters to the discussion in Sect. VI.

After passing another stage of internal review, we then finalized the analysis by updating the plots to show non-offset posteriors, computing tension and model comparison statistics, and writing descriptions of the results. After unblinding a few changes were made to the analysis: First, we discovered that our real-data results had accidentally been run using Pantheon [72] supernovae, so we reran all chains to include correct DES SNe data. While doing this, we additionally made a small change to our compressed Planck likelihood, centering its Gaussian likelihood on the full Planck chain's mean parameter values, rather than on maximum-posterior sample. This choice was motivated by the fact that sampling error in the maximum posterior estimate means that compressed likelihood is more accurate when centered on the mean. We estimate that centering on the maximum posterior sample was causing the compressed likelihood to be biased by $\sim 0.2\sigma$ relative to the mean, though we avoided looking at the direction of this bias in parameter space in order to prevent our knowledge of that direction from influencing this choice.

[7] The data combinations we use are slightly different than those in Ref. [1], so we simply require that our ΛCDM results be reasonably consistent with theirs, rather than identical.

B. Evaluating tensions and model comparison

There are two senses in which measuring tension is relevant for this analysis. First, we want to check for tension between different datasets in order to determine whether it is sensible to report their combined constraints. Second, we want to test whether our split-parameterization results are in tension with ΛCDM (or wCDM in the case of split w). For both of these applications, we evaluate tension using Bayesian suspiciousness [5, 122], which we compute using ANESTHETIC.[8] [123]

Suspiciousness S is a quantity built from the Bayesian evidence ratio R designed to remove dependence of the tension metric on the choice of prior. Let us define $S^{\rm dat}$ to measure the tension between two datasets A and B. The Bayesian evidence ratio between A and B's constraints is

$$R^{\rm dat} = \frac{\mathcal{Z}_{AB}}{\mathcal{Z}_A \mathcal{Z}_B}, \tag{21}$$

where $\mathcal{Z}_X = \int d\Theta\, \mathcal{P}(\Theta|X)$ is the Bayesian evidence for dataset X with posterior $\mathcal{P}(\Theta|X)$. Generally, values of $R^{\rm dat} > 1$ indicate agreement between A and B's constraints, while $R^{\rm dat} < 1$ indicates tension, though the translation of R values into tension probability depends on the choice of priors [5, 124].

The Kullback-Leibler (KL) divergence

$$\mathcal{D}_X = \int d\Theta\, \mathcal{P}(\Theta|X)\, \log\left[\mathcal{P}(\Theta|X)/\pi(\Theta)\right], \tag{22}$$

measures the information gain between the prior and the posterior for constraints based on dataset X. The comparison between KL divergences can be used to quantify the probability, given the prior, that constraints from datasets A and B will agree. This information is encapsulated in the information ratio,

$$\log I^{\rm dat} = \mathcal{D}_A + \mathcal{D}_B - \mathcal{D}_{AB}, \tag{23}$$

where $\mathcal{D}_{AB}$ is the KL divergence for the combined analysis of A and B. To get Bayesian suspiciousness we subtract the information ratio from the Bayesian evidence:

$$\log S^{\rm dat} = \log R^{\rm dat} - \log I^{\rm dat}. \tag{24}$$

[8] https://github.com/williamjameshandley/anesthetic

This subtraction makes S insensitive to changes in the choice of priors, as long as those changes do not significantly impact the posterior shape. As with R, larger values of S indicate greater agreement between datasets.

To translate this into a more quantitative measure of consistency, we use the fact that the quantity $d - 2\log S$ approximately follows a χ^2_d probability distribution, where d is the number of parameters constrained by both datasets. In practice we determine d by computing the Bayesian model dimensionality d [125], which accounts for the extent to which our posterior is unconstrained (prior-bounded) in some parameter-space directions. The model dimensionality for a single set of constraints X is defined as

$$\frac{\tilde{d}_X}{2} = \int d\Theta\, \mathcal{P}(\Theta|X)\, \left(\log\left[\mathcal{P}(\Theta|X)/\pi(\Theta)\right]\right)^2 - \mathcal{D}_X^2. \quad (25)$$

This measures the variance of the gain in information provided by X's posterior. Though $\tilde{d}$ is generally non-integer, it can be interpreted as the effective number of constrained parameters. To get the value of d that we use for our tension probability calculation, we compute

$$d \equiv d_{A\cap B} = \tilde{d}_A + \tilde{d}_B - \tilde{d}_{AB}. \quad (26)$$

Since any parameter constrained by either A or B will also be constrained by their combination, this subtraction will remove the count for any parameter constrained by only one dataset. Thus, d is the effective number of parameters constrained by both datasets. As we noted above, the quantity $d - 2\log S$ approximately follows a χ^2_d probability distribution, so we compute the tension probability

$$p(S > S^{\rm dat}) = \int_{d-2\log S}^{\infty} \chi^2_d(x)\, dx, \quad (27)$$

which quantifies the probability that the datasets A and B would be more discordant than measured. If in our analysis we find $p(S > S^{\rm dat}) < 5\%$, we will consider the two datasets to be in tension and will not report parameter constraints from their combination.

We will also use the Bayesian Suspiciousness in order to perform model comparison. One can interpret the Bayesian Evidence Ratio and Suspiciousness defined in Eqs. (21)- (24) as a test of the hypothesis that datasets A and B are described by a common set of cosmological parameters as opposed to two independent sets. That can be directly translated into what we would like to determine: are the data in tension with a single set of parameters describing both growth and geometric observables? We therefore compute

$$R^{\rm mod} = \mathcal{Z}_{\Lambda\rm CDM}/\mathcal{Z}_{\rm mod} \quad (28)$$

$$I^{\rm mod} = \mathcal{D}_{\Lambda\rm CDM} - \mathcal{D}_{\rm mod} \quad (29)$$

$$\log S^{\rm mod} = \log R^{\rm mod} - \log I^{\rm mod} \quad (30)$$

We use the label "mod" to identify these as model comparison statistics. As before we translate this into a tension probability by computing the Bayesian model dimensionality,

$$d = d_{\rm mod} - d_{\Lambda\rm CDM}, \quad (31)$$

and integrating the expected χ^2_d distribution as in Eq. (27). The resulting quantity $p(S > S^{\rm mod})$ measures the probability to exceed the observed tension between growth and geometric observables.

To convert a probability p to an equivalent $N\sigma$ scale, we compute N such that p is the probability that $|x| > N$ for a standard normal distribution,

$$p = 1 - 2\int_0^N (2\pi)^{-1/2} e^{-x^2/2}\, dx = \mathrm{erfc}\left(\tfrac{N}{\sqrt{2}}\right), \quad (32)$$

$$N = \sqrt{2}\,\mathrm{erfc}^{-1}(p). \quad (33)$$

Unless otherwise noted, this double-tail equivalent-probability is what will be used to convert probabilities to $N\sigma$. In the specific case when we are testing in Sect. V C whether the difference between the corresponding growth and geometry parameter is greater than zero, a single-tail probability is relevant instead; in that case, we simply multiply p in Eq. (33) by a factor of two.

V. RESULTS: SPLIT PARAMETERS

Here we present our main results, which are constraints on split parameters and an assessment of whether or not the data are consistent with $\Theta^{\rm grow} = \Theta^{\rm geo}$. Sect. V A reports results for splitting Ω_m (with $w = -1$), while results for splitting both Ω_m and w are presented in Sect. V B. We summarize the results in Sect. V D, reporting constraints, tension metrics, and model comparison statistics in Table III.

All datasets considered fulfill the $p(S > S^{\rm dat}) \geq 0.05$ prerequisite set in Sect. IV B for reporting combined constraints. Note, however, that while this is strictly true, the ΛCDM constraints from DES and Ext-geo, as well the split Ω_m constraints from DES and Ext-all are found to have tensions at the 2σ threshold. Thus, while we will report these combined results, they should be interpreted with caution.

Note that while one might assume that the 2σ tension found between DES and Ext-geo constraints in ΛCDM is related to the familiar Planck-DES σ_8 offset, this is not necessarily the case. This is because the σ_8 tension is generally studied in terms of the constraints from the full CMB power spectrum, while we are only using limited, geometric information from the CMB. When we do examine marginalized ΛCDM posteriors (not shown), we find substantial overlap between the 1σ regions of the marginalized DES and Ext-geo constraints on σ_8. Similarly, we find no obvious incompatibility between DES and Ext-geo constraints on any other individual parameter. This 2σ tension therefore appears to be related to the higher dimensional properties of the two posteriors.

A. Splitting Ω_m

Fig. 3 shows the 68 and 95% confidence regions for $\Omega_m^{\rm grow}$ and $\Omega_m^{\rm geo}$ for various data combinations. We study three different comparisons: a comparison between our fiducial DES dataset and a version without the BAO and SNe in the top panel; DES plus external geometric (DES+Ext-geo) data in the middle panel, and DES plus external data including RSD (Ext-all) in the bottom panel. The diagonal gray line corresponds to $\Omega_m^{\rm grow} = \Omega_m^{\rm geo}$. Marginalized parameter constraints and tension metrics for both data combination and model comparison are reported in Table III.

Looking at DES-only results in the top panel, we find that, as expected including the (geometric) DES BAO and SNe likelihoods tighten the constraints on $\Omega_m^{\rm geo}$ but only weakly affect $\Omega_m^{\rm grow}$. We find that constraints on $\Omega_m^{\rm geo}$ are much stronger than those on $\Omega_m^{\rm grow}$ for both the 3×2pt-only and the fiducial DES constraints. In fact, the DES constraints on $\Omega_m^{\rm geo}$ are only slightly weaker than ΛCDM constraints on Ω_m, implying that most of DES' constraining power is derived from geometric information. This might be surprising, since one might expect a LSS survey to have more growth sensitivity. However, it is consistent with the findings summarized in Ref. [39], which discusses how distance and growth factor measurements can place comparable constraints on the dark energy equation of state when other cosmological parameters are held fixed [37, 38], but the growth weakens when one marginalizes over more parameters [28, 35]. The fact that the confidence regions intersect the $\Omega_m^{\rm grow} = \Omega_m^{\rm geo}$ line but are asymmetrically distributed around it is reflected in the Bayesian Suspiciousness measurement of 1.5σ tension with ΛCDM.

In the middle panel of Fig. 3 we show the combination of the DES data with external geometric measurements from the CMB and BAO (Ext-geo). As expected, the external geometric data alone put tight constraints on $\Omega_m^{\rm geo}$ but do not constrain $\Omega_m^{\rm grow}$ at all. The combined constraints on $\Omega_m^{\rm geo}$ are straightforwardly dominated by those from the external data, while the DES+Ext-geo constraints on $\Omega_m^{\rm grow}$ are counterintuitively bounded from below but not above. To understand the appearance of the lower bound, note that the DES-only measurement of a given late-time density fluctuation amplitude allows arbitrarily small values of $\Omega_m^{\rm grow}$ because little or no structure growth over time can be compensated by a large primordial amplitude $A_{\rm s}$. Adding the Planck constraints provides an early-time anchor for $A_{\rm s}$, and therefore requires $\Omega_m^{\rm grow}$ to be above some minimal value in order to account for the evolution of structure growth between recombination and the redshifts probed by DES. The reason DES' upper bound on $\Omega_m^{\rm grow}$ does not translate to the DES+Ext-geo constraints can also be understood in terms of degeneracies in our model's larger parameter space. We will explore this in more detail in Sect. VI.

Finally, the bottom panel of Fig. 3 shows constraints from DES and Ext-all, which adds BOSS RSD con-

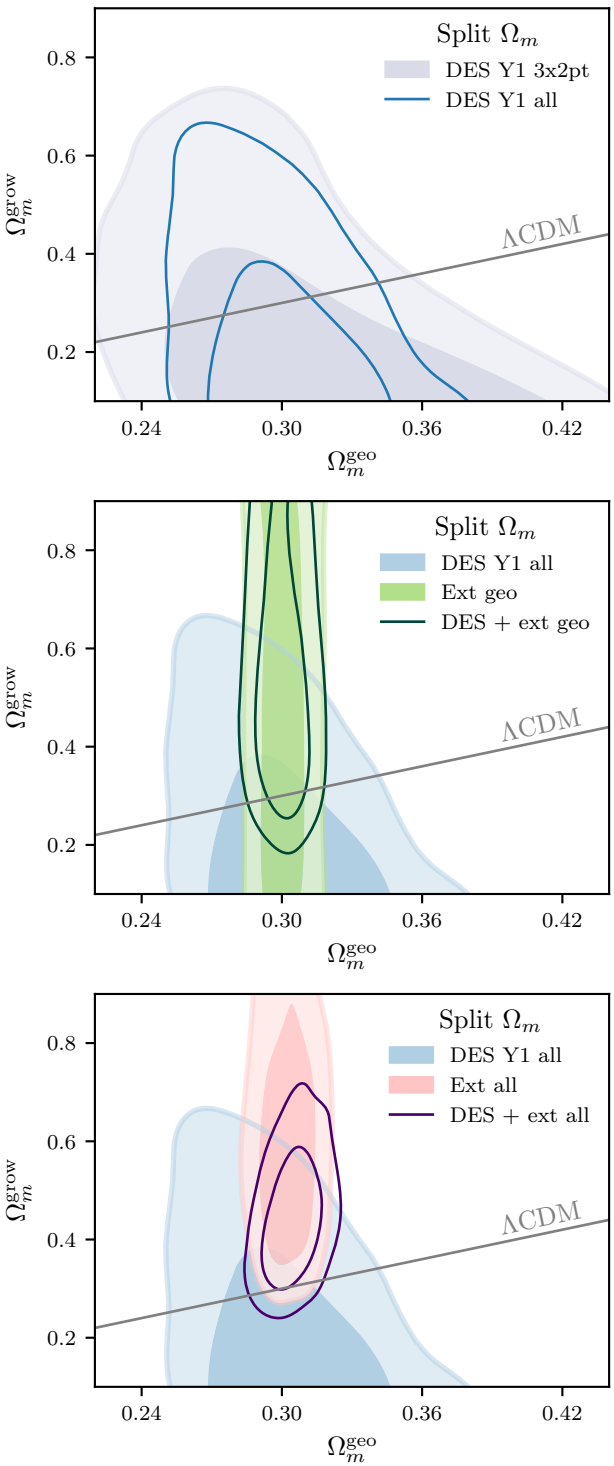

FIG. 3. The 68 and 95% confidence regions for $\Omega_m^{\rm grow}$ and $\Omega_m^{\rm geo}$ for our various data combinations. The diagonal gray lines show where $\Omega_m^{\rm grow} = \Omega_m^{\rm geo}$. Note that the three plots have the same axis ranges, and that vertical axes cover a much larger range of values than the horizontal axes. The blue outline-only contours in the top plot are the same as the shaded blue contours in the other plots.

straints on growth to the previously considered external geometric measurements. We see that compared to the middle panel's Ext-geo results, adding RSD allows Ext-all to place a lower bound on $\Omega_m^{\rm grow}$, and when combined with DES, $\Omega_m^{\rm grow}$ is bounded on both sides. The fact that there is not very much overlap between the DES and Ext-all contours, with Ext-all preferring somewhat higher $\Omega_m^{\rm grow}$ than DES, reflects their weak 2σ tension. The shape of the Ext-all constraints here, as well as how DES adds information, is related to a degeneracy between $\Omega_m^{\rm grow}$ and $\sum m_\nu$, which we will discuss further in Sect. VI.

B. Splitting Ω_m and w

Fig. 4 shows the 68% and 95% confidence contours when splitting both Ω_m and w for DES+Ext-all constraints, showing the parameters $\Omega_m^{\rm geo}$, $\Omega_m^{\rm grow}$, $w^{\rm geo}$, and $w^{\rm grow}$. The most notable feature is the strong degeneracy between the two growth parameters, $\Omega_m^{\rm grow}$ and $w^{\rm grow}$. We interpret this to mean that while DES+Ext-all can separately constrain growth and geometry, the data cannot distinguish between Ω_m-like and w-like deviations from the structure growth history expected from wCDM. This behavior is also consistent with Ref. [27]'s finding that, for a given $\Omega_m(z)$, w only weakly effects growth rates. This makes it unsuprising that it is difficult to robustly constrain $w^{\rm grow}$ separately from $\Omega_m^{\rm grow}$.

Because of this degeneracy, even using our most informative "DES+Ext-all" data combination $w^{\rm grow}$ is unconstrained, and the upper and lower bounds placed on $\Omega_m^{\rm grow}$ are entirely dependent on the choice of prior for $w^{\rm grow}$. As discussed in Appendix B, our analyses of simulated data showed that projection effects associated with this degeneracy significantly affect the one-dimensional marginalized constraints on both $\Omega_m^{\rm grow}$ and $w^{\rm grow}$. Because of this we do not report parameter constraints for this model.

C. Consistency with $\Theta^{\rm grow} = \Theta^{\rm geo}$

Ultimately the question we would like to ask is whether the results above are consistent with ΛCDM, or with wCDM, in the case where we split both Ω_m and w. There are several ways we can assess this. We begin simply by looking at the two-dimensional confidence regions shown in Figs. 3 and 4, noting whether or not they intersect the lines corresponding to ΛCDM (in Fig. 3) and wCDM (in Fig. 4). We see that when we split Ω_m, the 68% confidence intervals for DES and DES+Ext-geo intersect the $\Omega_m^{\rm grow} = \Omega_m^{\rm geo}$ line, while that of DES+Ext-all just touches the ΛCDM line, preferring $\Omega_m^{\rm grow} > \Omega_m^{\rm geo}$. When we split both Ω_m and w, both the $\Omega_m^{\rm grow} = \Omega_m^{\rm geo}$ and $w^{\rm grow} = w^{\rm geo}$ lines goes directly through the DES+Ext-all 68% confidence intervals.

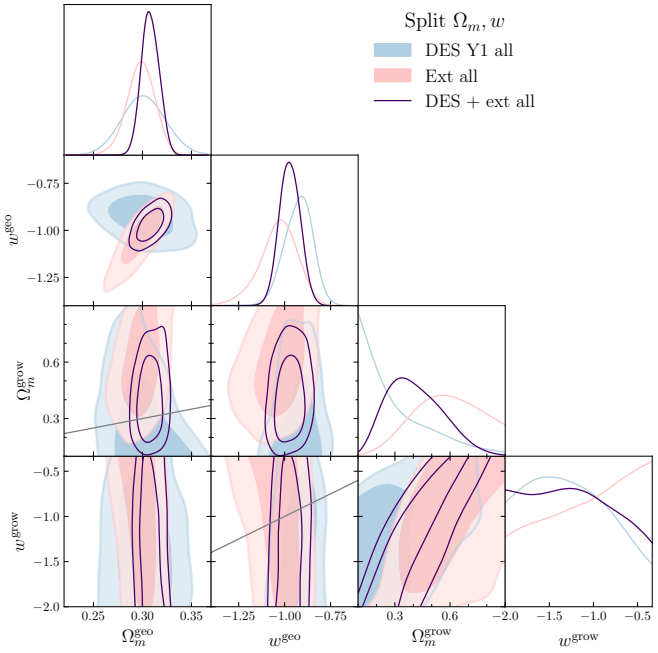

FIG. 4. Marginalized constraints from DES and external data when both Ω_m and w are split. The diagonal panels show normalized one-dimensional marginalized posteiors, while the off-diagonal panels show 68% and 95% confidence regions. Solid gray lines show the wCDM parameter subspace where $\Omega_m^{\rm grow} = \Omega_m^{\rm geo}$ and $w^{\rm grow} = w^{\rm geo}$.

To assess consistency with $\Theta^{\rm grow} = \Theta^{\rm geo}$ in our full parameter space, we use Bayesian Suspiciousness $S^{\rm mod}$, as described in Eq. (30) of Sect. IV B. As we did when we used Suspiciousness to evaluate concordance between datasets, we use $p(S > S^{\rm mod})$ to report the probability to exceed the observed Suspiciousness, and "1-tail equiv. σ" as the number of normal distribution standard deviations with equivalent-probability. Here, larger $S^{\rm mod}$, smaller $p(S > S^{\rm mod})$, and larger σ indicate more tension with $\Theta^{\rm grow} = \Theta^{\rm geo}$. Numbers for all of these quantities are shown in Table III. According to this metric, when we split Ω_m we find the DES-only results to have a 1.5σ tension with ΛCDM. This becomes 1.9σ for DES+Ext-geo, and 1.0σ for DES+Ext-all. When we split both Ω_m and w we find tensions with wCDM to be 1.6σ for DES-only and 1.4σ for DES+Ext-all.

As another way of quantifying compatibility of the split-Ω_m constraints with ΛCDM, in Fig. 5 we show the marginalized posterior for the difference $\Omega_m^{\rm grow} - \Omega_m^{\rm geo}$. When we assess the fraction of the posterior volume above and below 0, we find that the fraction of the posterior volume with $\Omega_m^{\rm grow} > \Omega_m^{\rm geo}$ is 30% for DES-only, equivalent to a normal distribution single-tail probability of 0.5σ. These numbers become 91% (1.3σ) for DES+Ext-geo, and 95% (1.6σ) for DES+Ext-all.

We note two points of caution in interpreting the $\Omega_m^{\rm grow} - \Omega_m^{\rm geo}$ marginalized posterior. First, because of the difference in constraining power on $\Omega_m^{\rm grow}$ and $\Omega_m^{\rm geo}$

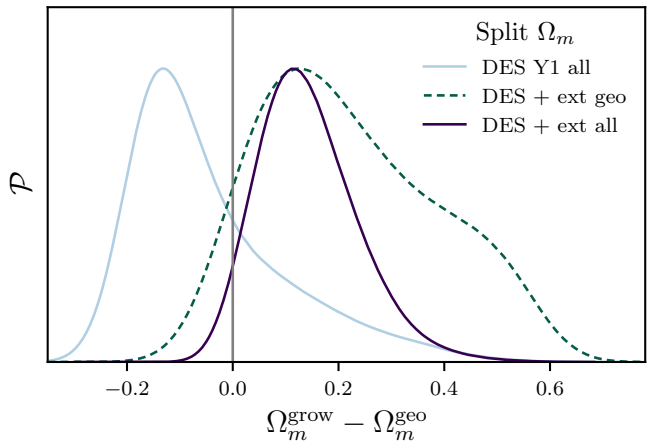

FIG. 5. Marginalized posterior of the difference $\Omega_m^{\rm grow} - \Omega_m^{\rm geo}$, from fitting the split-Ω_m model to the DES, DES+Ext-geo, and DES+Ext-all data combinations.

there is some asymmetry expected in these marginalized posteriors even if the data are consistent with ΛCDM. This can be seen in Fig. 12 of Appendix C, which shows versions of this plot for synthetic data generated with $\Omega_m^{\rm grow} = \Omega_m^{\rm geo}$. Additionally, the posterior distribution is impacted by the priors on $\Omega_m^{\rm grow}$ and $\Omega_m^{\rm geo}$. While the GetDist software allows us to correct for the impact of hard prior boundaries for the parameters we sample over, it is unable to do so for derived parameters. This means that in cases where the shape of the posterior is influenced by the prior boundary of e.g. $\Omega_m^{\rm grow}$, this will necessarily affect the shape of the marginalized posterior for $\Omega_m^{\rm grow} - \Omega_m^{\rm geo}$. Accounting for these caveats and comparing to the simulated results in Appendix C, we see that the DES+Ext-all probability distribution is shifted to higher $\Omega_m^{\rm grow} - \Omega_m^{\rm geo}$ than was found in simulated analyses. The DES-only and DES+Ext-geo distributions do not appear to be significantly different from what might be expected given parameter space projection effects in ΛCDM.

D. Summary of main results

The results discussed in this section are summarized in Table III. In it, for the split Ω_m model we show one-dimensional marginalized constraints on $\Omega_m^{\rm grow}$ and $\Omega_m^{\rm geo}$ from DES+Ext-geo and DES+Ext-all, along with ΛCDM and wCDM constraints for comparison. For each parameter we show two-sided errors corresponding to the 68% confidence interval one-dimensional marginalized posterior. Because we expect the one-dimensional marginalized posteriors to be subject to significant projection effects for DES-only constraints on the split Ω_m model and for the DES+Ext-all constraints when splitting both Ω_m and w, as discussed in Sect. IV and Appendix B we do not report parameter bounds for those cases.

TABLE III. Summary of results. Parameter errors quoted are 68% confidence intervals, and $\tilde{d}$ is the Bayesian model dimensionality. The quantity S is Bayesian Suspiciousness, with superscript "dat" denoting an assessment of tension between two datasets, and "mod" denoting model comparison.

ΛCDM	DES	DES+Ext-geo	DES+Ext-all
Ω_m	$0.296^{+0.020}_{-0.022}$	$0.301^{+0.009}_{-0.008}$	$0.302^{+0.007}_{-0.008}$
$\tilde{d}$	14.0 ± 0.7	18.2 ± 0.8	15.8 ± 0.8
$\log S^{\rm dat}$	-	-1.8 ± 0.3	-0.8 ± 0.2
$p(S > S^{\rm dat})$	-	0.04 ± 0.03	0.25 ± 0.05
equiv. σ	-	2.0 ± 0.4	1.2 ± 0.1

Split Ω_m	DES	DES+Ext-geo	DES+Ext-all
$\Omega_m^{\rm grow} - \Omega_m^{\rm geo}$	-	$0.126^{+0.228}_{-0.129}$	$0.116^{+0.100}_{-0.084}$
$\Omega_m^{\rm geo}$	-	$0.300^{+0.009}_{-0.008}$	$0.304^{+0.009}_{-0.008}$
$\Omega_m^{\rm grow}$	-	$0.425^{+0.232}_{-0.131}$	$0.421^{+0.102}_{-0.089}$
$\tilde{d}$	15.0 ± 0.7	18.1 ± 0.9	19.8 ± 1.0
$\log S^{\rm dat}$	-	-1.1 ± -0.2	-2.0 ± 0.3
$p(S > S^{\rm dat})$	-	0.13 ± 0.06	0.05 ± 0.03
equiv. σ	-	1.5 ± 0.3	2.0 ± 0.3
$\log S^{\rm mod}$	-0.6 ± 0.2	-1.3 ± 0.2	-0.4 ± 0.3
$p(S > S^{\rm mod})$	0.14 ± 0.08	0.06 ± 0.05	0.31 ± 0.07
equiv. σ	1.5 ± 0.4	1.9 ± 0.4	1.0 ± 0.1
$p(\Omega_m^{\rm grow} > \Omega_m^{\rm geo})$	0.30	0.91	0.95
1-tail equiv. σ	0.5	1.3	1.6

wCDM	DES	DES+Ext-all
Ω_m	$0.292^{+0.022}_{-0.022}$	$0.301^{+0.009}_{-0.008}$
w	$-0.911^{+0.073}_{-0.076}$	$-0.997^{+0.048}_{-0.050}$
$\tilde{d}$	16.3 ± 0.8	17.6 ± 0.8
$\log S^{\rm dat}$	-	-1.5 ± 0.2
$p(S > S^{\rm dat})$	-	0.17 ± 0.04
equiv. σ	-	1.4 ± 0.1

Split Ω_m, w	DES	DES+Ext-all
$\tilde{d}$	15.2 ± 0.7	18.2 ± 0.9
$\log S^{\rm dat}$	-	-2.2 ± 0.2
$p(S > S^{\rm dat})$	-	0.09 ± 0.03
equiv. σ	-	1.7 ± 0.2
$\log S^{\rm mod}$	-0.5 ± 0.2	-0.6 ± 0.2
$p(S > S^{\rm mod})$	0.11 ± 0.07	0.15 ± 0.09
equiv σ	1.6 ± 0.4	1.4 ± 0.4

For all model-data combinations considered we use Bayesian Suspiciousness as defined in Sect. IV B to report data tension and model comparison statistics. In Table III, $\tilde{d}$ is the Bayesian model dimensionality (Eq. (25)) quantifying the effective number of parameters constrained, $S^{\rm dat}$ is the Bayesian suspiciousness as-

sessing agreement between pairs of datasets (Eq. (24)), and $S^{\rm mod}$ is the model-comparison Bayesian Suspiciousness (Eq. (30)), quantifying tension or agreement with $\Theta^{\rm grow} = \Theta^{\rm geo}$. The quantities $p(S > S^X)$, for $X \in [{\rm dat}, {\rm mod}]$ is the probability that a random realization exceeds the observed Suspiciousness S^X, and "equiv. σ" translates that probability into the number standard deviations with an equivalent double-tail probability for a normal distribution (Eq. (33)). Large S, small p, and large equivalent σ indicate tension, while small S, large p, and small equivalent σ indicate concordance. For all quantities the numbers quoted in Table III are the mean and standard deviation from sampling error reported by ANESTHETIC.

As an alternative model-comparison statistic for the split-Ω_m model, we additionally report $p(\Omega_m^{\rm grow} > \Omega_m^{\rm geo})$, the fraction of the posterior volume with $\Omega_m^{\rm grow} > \Omega_m^{\rm geo}$. For this part of the table, the "equiv. σ" is the number of normal distribution standard deviations with equivalent single-tail probability.

VI. RESULTS: IMPACT OF GROWTH-GEOMETRY SPLIT ON OTHER PARAMETERS

Here we explore how our split parameterization, focusing on splitting only Ω_m, affects the inference of other cosmological parameters. In this discussion we will primarily reference Fig. 6, which shows two-dimensional marginalized posteriors of DES+Ext-all constraints on $\Omega_m^{\rm grow}$, $\Omega_m^{\rm geo}$, the difference $\Omega_m^{\rm grow} - \Omega_m^{\rm geo}$, $\sum m_\nu$, $S_8 \equiv \sigma_8\sqrt{\Omega_m^{\rm geo}/0.3}$, h, and $A_{\rm IA}$. For comparison, we also show a DES+Ext-geo version of this plot in Fig. 17 of Appendix E. We use this higher dimensional visalization of the posterior to characterize how additional degrees of freedom in the relationship between expansion history and structure growth changes considerations in cosmological analyses, both in terms of how we model of astrophysical effects ($\sum m_\nu$, $A_{\rm IA}$) and in terms of commonly studied tensions (S_8, h).

In the off-diagonal panels of Fig. 6, 68% and 95% confidence regions are shown for DES-only as blue shaded contours, Ext-all as pink shaded contours, and the combination DES+Ext-all as dark purple outlines. The diagonal panels show normalized one-dimensional marginalized posteriors for each parameter. Solid gray lines show the ΛCDM subspace where $\Omega_m^{\rm grow} = \Omega_m^{\rm geo}$, and grey dashed lines show the DES+Ext-all posterior for ΛCDM.

A. Effect of split on neutrino mass

Because the combination of Planck, BOSS BAO, and BOSS RSD are able to tightly constrain cosmological parameters in ΛCDM, it may be surprising that DES adds information at all when combined with the Ext-all data. Looking at Fig. 6, we see that it does so because the external data exhibits a significant degeneracy between $\Omega_m^{\rm grow}$ and the sum of neutrino masses $\sum m_\nu$. The Ext-all degeneracy occurs because changes in $\sum m_\nu$ and $\Omega_m^{\rm grow}$ have competing effects on the matter power spectrum: higher neutrino mass suppresses structure formation at small scales ($k \gtrsim 10^{-2} h$ Mpc^{-1}), while raising $\Omega_m^{\rm grow}$ results produces more late-time structure. DES data adds constraining power because it provides an upper bound on $\Omega_m^{\rm grow}$ which breaks that degeneracy.

Looking at the marginalized constraints on $\sum m_\nu$, we see that both the DES+Ext-all (Fig. 6) and DES+Ext-geo (Fig. 17) constraints produce a detection of neutrino mass at $\sum m_\nu = 0.4 \pm 0.1$ eV, which is significantly higher than the upper bounds obtained from the combined analysis of BOSS DR12 and the full Planck temperature and polarization power spectra [49, 57]. The DES-only posterior gives a weak lower bound on neutrino mass, though we suspect that this may be at least in part caused by parameter-space projection effects. In ΛCDM, the Ext-all constraints on $\sum m_\nu$ become an upper bound of $\sum m_\nu < 0.45$ eV at 95% confidence, which is is consistent with the BOSS results (though weaker because we do not use the full Planck likelihood), while the DES preference for high $\sum m_\nu$ remains. This causes the DES+Ext-all ΛCDM posterior, shown as a gray dashed line in Fig. 6, to peak at $\sum m_\nu = 0.2 \pm 0.1$ eV.

To begin interpreting the preference for high $\sum m_\nu$, we can look at the $\sum m_\nu$-$\Omega_m^{\rm grow}$ panel of Fig. 6 and note that the Ext-all constraints exhibit a preference for the high-$\sum m_\nu$, high-$\Omega_m^{\rm grow}$ part of parameter space. That preference combined with the DES upper bound on $\Omega_m^{\rm grow}$ likely drives the 2σ tension between Ext-all and DES and appears to be responsible for pulling the combined DES+Ext-all constraints away from the ΛCDM $\Omega_m^{\rm grow} = \Omega_m^{\rm geo}$ line.

It is instructive to examine how the constituent Planck and BOSS likelihoods combine to produce the Ext-all contours. We show this in Fig. 7, with the compressed Planck posterior in yellow, BOSS BAO+RSD in orange, and their combination, Ext-all, as black outlines. The compressed Planck likelihood approximately defines a plane in the σ_8-$\sum m_\nu$-$\Omega_m^{\rm grow}$ parameter space because Planck's measurement of $A_{\rm s}$ can be extrapolated forward to predict σ_8, but the effects of $\Omega_m^{\rm grow}$ and $\sum m_\nu$ on late-time structure growth loosen that predictive relationship. The BOSS data probe late-time structure more directly, so the combined BAO and RSD results can be thought of as roughly providing a measurement of σ_8 that is insensitive to $\sum m_\nu$ and only weakly dependent on $\Omega_m^{\rm grow}$.

Putting all of this together, we see that the shape of the Ext-all posterior strongly depends on the relationship between Planck's measurement of $A_{\rm s}$, BOSS's measurement of σ_8, as well as the extent to which late-time degrees of freedom impact how deterministically Planck's $A_{\rm s}$ constraint maps to σ_8. For example: if the Planck $A_{\rm s}$ constraints were lowered slightly, or the BOSS σ_8 constraints were raised, this would move the Ext-all constraints towards lower $\sum m_\nu$ and consequently, lower $\Omega_m^{\rm grow}$. The

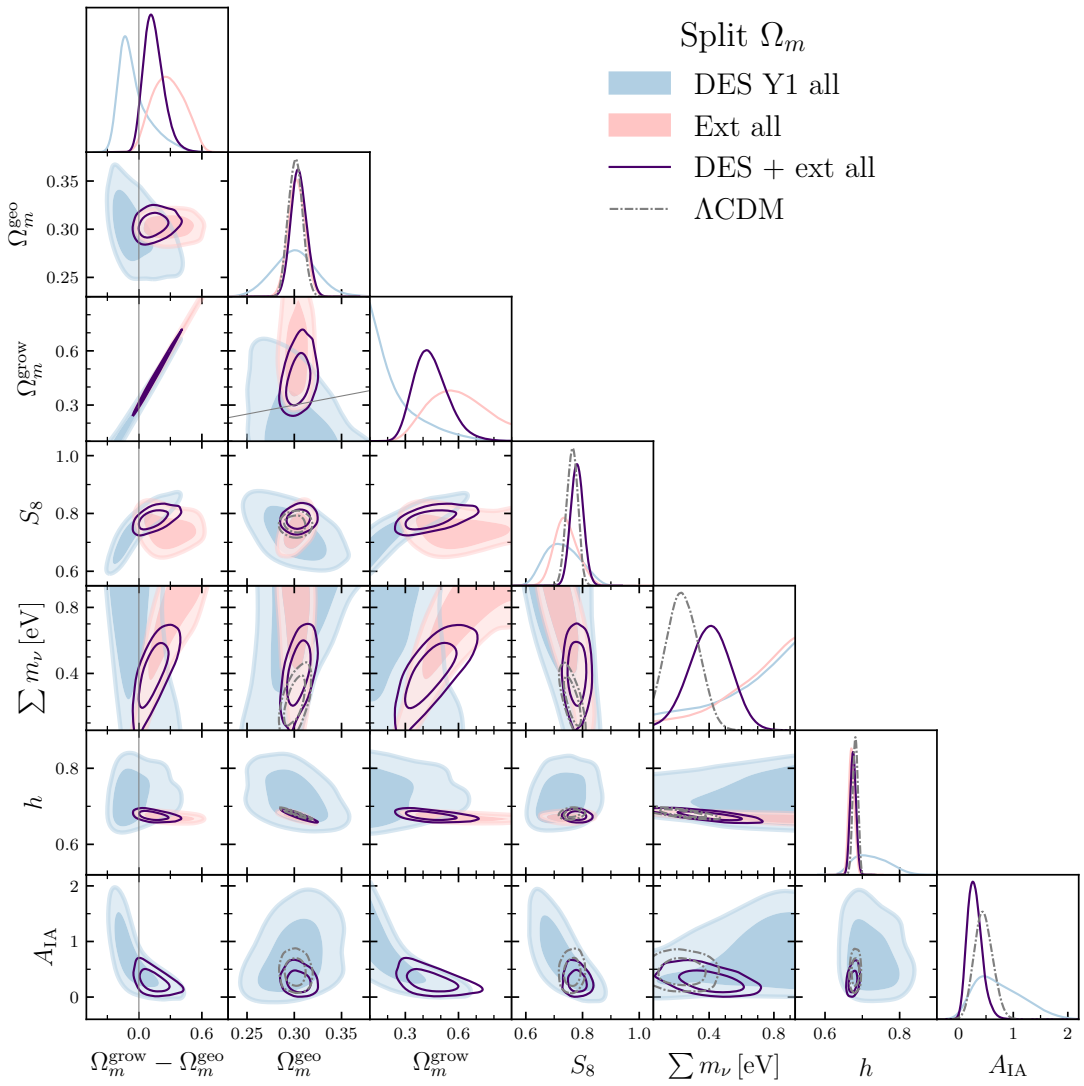

FIG. 6. Constraints from the DES and the Ext-all external dataset, which includes the compressed Planck likelihood, BOSS DR12 BAO, and BOSS DR12 RSD. The off-diagonal panels show the 68 and 95% confidence intervals for each data combination, while the diagonal panels show normalized one-dimensional marginalized posteriors on parameters. DES-only results are shown in blue, Ext-all results are pink, and their combination is shown using unshaded purple contours. The gray dashed curves show DES+Ext-all constraints in ΛCDM and the gray solid lines show where $\Omega_m^{\rm grow} = \Omega_m^{\rm geo}$.

DES+Ext-geo constraints have a similar property: we can see in the S_8-$\sum m_\nu$ panel of Fig. 17 that slight relative changes to the Planck $A_{\rm s}$ or DES S_8 constraints can have a significant impact on the $\sum m_\nu$ posterior. In other words, our results' preference for high $\sum m_\nu$ (and consequently, high $\Omega_m^{\rm grow}$) can be interpreted as a manifestation of the early-versus-late-Universe σ_8 tension discussed in the Introduction.

Our findings here are in line with several previous studies which report a preference for $\sum m_\nu \sim 0.3\,{\rm eV}$ when modeling degrees of freedom affecting structure growth are introduced to combined CMB and LSS analyses. These include the growth-geometry split analysis of Refs. [41, 42], as well as examinations of neutrino mass in conjunction with $A_{\rm Lens}$ [126, 127] (which describes the amount of lensing-induced smoothing of the CMB power spectrum), time dependent dark energy [128], and modified gravity [129]. Notably, however, these results are in contrast with those documented in Fig. 19 of the official BOSS DR12 analysis paper [49], which show that BOSS DR12 BAO and RSD combined with Planck temperature and polarization are able to constrain $\sum m_\nu < 0.25\,{\rm eV}$ at 95% confidence, even when marginalizing over $A_{\rm Lens}$ and a free amplitude multiplying $f\sigma_8$. Our Ext-all constraints are weaker than this because using a compressed Planck likelihood causes us to lose information about a degeneracy between $\sum m_\nu$ and the shift parameter R that is present in the full likelihood (which in the BOSS analysis is broken by BAO angular diameter distance measurements), and potentially also because our

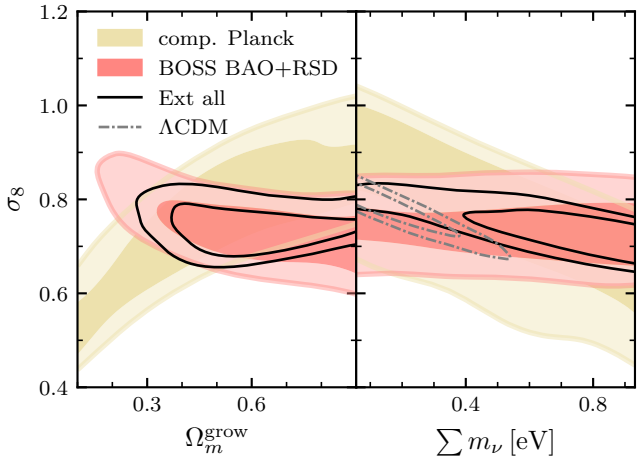

FIG. 7. Constraints on parameters most relevant for describing late-time growth, shown for the datasets that make up Ext-all. Contours show the 68% and 95% confidence regions for the compressed Planck likelihood in yellow and for BOSS DR12 BAO and RSD in orange. The unshaded black contours correspond to Ext-all, and are the same as the pink contours in other Figures. Gray dashed contours show ΛCDM results for Ext-all.

choice of priors requires $\sum m_\nu > 0.06$ eV while BOSS uses $\sum m_\nu > 0$ eV.

To explore how our results would be affected by tighter $\sum m_\nu$ constraints, in Fig. 8 we show DES+Ext-geo and DES+Ext-all constraints on $\Omega_m^{\rm grow}$ and $\Omega_m^{\rm geo}$ when the sum of neutrino masses is fixed to its minimal value, 0.06 eV. Additionally, in Appendix E 2 Fig. 18 shows how either fixing $\sum m_\nu$ or requiring $\Omega_m^{\rm grow} = \Omega_m^{\rm geo}$ alters the Ext-all constraints (without DES data), and Table IV reports fixed-$\sum m_\nu$ versions of our data and model tension metrics. We find that assuming minimal neutrino mass allows us to constrain $\Omega_m^{\rm grow}$ with either DES+Ext-geo alone or just the Ext-all data, and that the fixed-neutrino-mass DES+Ext-all constraints are dominated by information from the external data. For all data combinations, fixing neutrino mass improves the agreement between datasets, and the split-Ω_m constraints become consistent with ΛCDM at the $< 1\sigma$ level.

B. Effect of split on S_8

In examining the effect of the growth-geometry split parameterization on σ_8, we can orient ourselves by making a few observations. First, as noted in Sect. II B, the usual negative degeneracy between Ω_m and σ_8 seen in weak-lensing analyses appears in the DES-only constraints here as a degeneracy between $\Omega_m^{\rm geo}$ (which appears in the lensing prefactor of the lensing kernel) and σ_8. Thus, to more easily compare to results in other papers, in Fig. 6 we show constraints on $S_8 = \sigma_8\sqrt{\Omega_m^{\rm geo}/0.3}$.

In contrast, the DES-only constraints on $\Omega_m^{\rm grow}$ and σ_8 are positively correlated. This might seem counterintuitive because changing $\Omega_m^{\rm grow}$ and changing $A_{\rm s}$ have similar effects on the matter power spectrum, and we are used to thinking of σ_8 as equivalent to $A_{\rm s}$. However, it is important to remember that splitting growth and geometry breaks our usual intuition about the one-to-one relationship between $A_{\rm s}$ and σ_8. While $\Omega_m^{\rm grow}$ and $A_{\rm s}$ do indeed have a negative degeneracy (see Fig. 10), $\Omega_m^{\rm grow}$ and σ_8 do not. Because σ_8 is a derived parameter obtained by integrating the power spectrum, and increasing $\Omega_m^{\rm grow}$ raises the amplitude of the power spectrum, if all other parameters are fixed, raising $\Omega_m^{\rm grow}$ will produce an increase in σ_8. Thus, the degeneracy we find between $\Omega_m^{\rm grow}$ and σ_8 is expected for the same reason that we generally expect a positive correlation between $A_{\rm s}$ and σ_8.

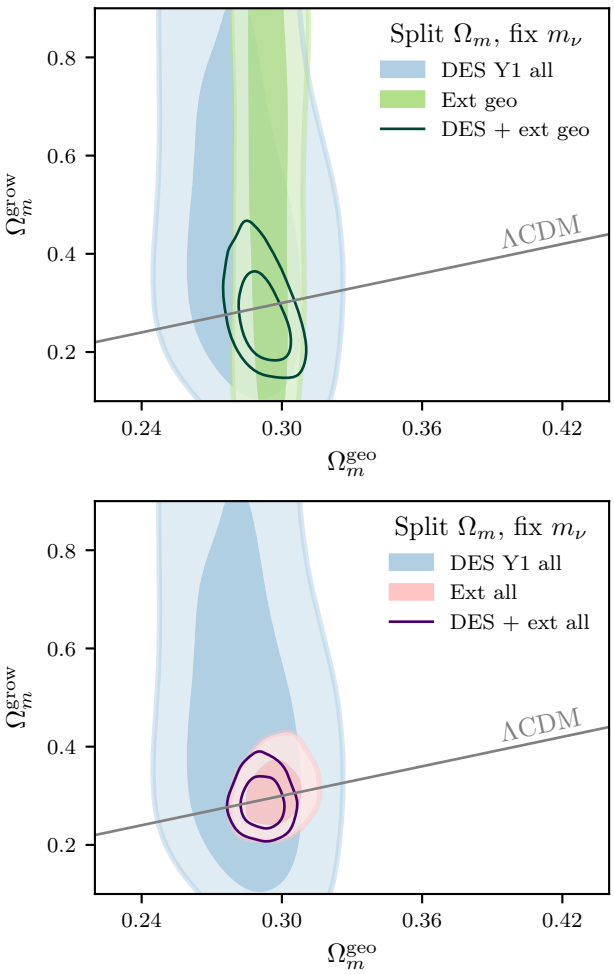

FIG. 8. The same combined DES+Ext-geo (top) and DES+Ext-all (bottom) constraints as the second and third panels of Fig. 3, but with the sum of neutrino masses fixed to 0.06 eV.

Compared to ΛCDM, splitting Ω_m has relatively little effect on the DES+Ext-all S_8 constraints, while it weakens and shifts those from DES and DES+Ext-geo. These S_8 values remain consistent with the DES Y1-3×2pt ΛCDM result of $0.773^{+0.026}_{-0.020}$ and below the full

Planck ΛCDM constraint of $0.842^{+0.027}_{-0.025}$ [4]. We note that the DES+Ext-geo constraint on S_8 moves upwards enough to be consistent with the ΛCDM Planck result, while the DES estimate moves further away — albeit, more by reducing the lower bound than by ruling out values preferred in by DES ΛCDM. This behavior is qualitatively similar to the S_8 constraint in the DES Y1-3×2pt the $\Sigma - \mu$ modified gravity model analysis of Ref. [31].

We find no disagreement between DES and the external data's marginalized S_8 constraints, which might suggest that our growth-geometry split is able to resolve the σ_8 tension. However, this interpretation is confounded by the fact that we use more limited information from Planck than standard analyses. The compressed Planck likelihood we use does not contain any information from the lensing smoothing of CMB power spectrum peaks, it is unable to constrain neutrino mass on its own, and so it exhibits a negative S_8-$\sum m_\nu$ degeneracy. This causes the DES and Ext-geo marginalized posteriors on S_8 to be compatible even in ΛCDM. In other words, we can concretely say that the Planck preference for high S_8 compared to DES and other probes of LSS relies on on information from the CMB that is not included in the geometry-only compressed likelihood.

C. Effect of split on H_0

We find that in our split parameterization, the constraints on $h \equiv H_0/(100\,\mathrm{km\,s^{-1}\,Mpc^{-1}})$ do not significantly change relative to what they are in ΛCDM. The Planck likelihood provides nearly all the information on h, with its $\Omega_m h^2$ constraint manifesting as a tight ellipse in the $\Omega_m^{\rm geo}$-h planes of both Fig. 6 and 17. This suggests that non-standard structure growth will have little impact on the value of the Hubble constant inferred from the data we consider, and therefore is a poor candidate for resolving the H_0 tension.

D. Effect of split on $A_{\rm IA}$

Finally, we examine how opening up our split parameter space impacts constraints on the amplitude of intrinsic alignments. We can see in Fig. 6 that there is a significant negative degeneracy between $\Omega_m^{\rm grow}$ and $A_{\rm IA}$ present in the DES posterior. This occurs because the factor of ρ_{m0} in Eq. (6) makes the contribution of intrinsic alignments signal proportional to the product $\Omega_m^{\rm grow} A_{\rm IA}$. As we discuss in Sect. IV A and Appendix B, we believe this degeneracy is why our growth-focused beyond-ΛCDM parameterization is more sensitive to assumptions about the redshift dependence of intrinsic alignments than the other extensions to ΛCDM considered in Ref. [31].

Like the previous DES Y1 papers [4, 130, 131], we are not able to constrain the redshift power-law slope α_{IA}, but we are able to constrain the amplitude $A_{\rm IA}$. For comparison, in ΛCDM, our DES, DES+Ext-geo, and DES+Ext-all posteriors all give $A_{\rm IA} = 0.4 \pm 0.2$, which is compatible with (and about twice as constraining as) what reported in Ref. [4] for DES Y1-3×2pt. When we split Ω_m, the $\Omega_m^{\rm grow}$-$A_{\rm IA}$ degeneracy causes the DES-only constraints to widen considerably, with the bulk of the posterior volume residing in the region with small $\Omega_m^{\rm grow}$ and high $A_{\rm IA}$. Combining external data places a lower bound on $\Omega_m^{\rm grow}$, which breaks the degeneracy and restricts $A_{\rm IA}$ to small values. In fact, DES+Ext-geo and DES+Ext-all constraints on $A_{\rm IA}$ are slightly tighter and peak at slightly lower values in our split parameterization compared to ΛCDM. We observe a slight negative degeneracy between $A_{\rm IA}$ and $\sum m_\nu$ in these combined posteriors, so it is possible that this is caused by the same properties of the data which drive the high $\sum m_\nu$ results.

VII. DISCUSSION

We perform a combined analysis of DES Y1 galaxy clustering and weak lensing, DES Y1 BAO, and DES Y3 supernovae measurements in which we split cosmological parameters related to the physics of dark energy into separate "growth" and "geometry" versions. In this growth-geometry split analysis, the geometry parameters $\Theta^{\rm geo}$ enter model predictions for observables related to expansion history, including all distances, the shape of the high-z matter power spectrum, and projection operations used to convert the three-dimensional power spectrum to observed 2PCF. The growth parameters, in turn, enter calculations of late-time structure growth: $\Theta^{\rm grow}$ are used to compute the linear and non-linear evolution of the matter power spectrum at late times as well as intrinsic alignment contributions to shear correlations.

We primarily focus on splitting Ω_m, and our main results are reported based on two data combinations: DES+Ext-geo, which combines the DES measurements with external geometric information from BOSS DR12 BAO and a compressed Planck 2015 likelihood, and DES+Ext-all, which additionally includes BOSS DR12 RSD measurements as an external probe of structure growth. To supplement these main results, we also consider secondary data-model combinations which are less robust to changes in our modeling assumptions but can still aid in the interpretation of the main results: DES-only constraints on split Ω_m, and DES+Ext-geo constraints when splitting both Ω_m and w. We stress-test our analysis procedure by ensuring that the results are not biased in the presence of a sample of injected systematic errors, and perform a blinded analysis; see Sec. IV A for details.

We use these analyses to address the questions raised in the introduction, which we now answer in order.

A. Are DES constraints informed more by growth or geometric information?

For all data combinations considered, we find constraints on geometric parameters to be much tighter than those on growth parameters (Fig. 3). Thus, at least in the context of how we have defined growth and geometric observables, DES constraints are more informed by geometry than by a direct measurement of the evolution of structure growth. This is both because changing $\Omega_m^{\rm grow}$ has a smaller effect on the matter power spectrum than $\Omega_m^{\rm geo}$ (see Fig. 1), and because of parameter degeneracies impacting the $\Omega_m^{\rm grow}$ constraints. As seen in Fig. 1, changing $\Omega_m^{\rm grow}$ results in a nearly scale-independent amplitude change to $P(k)$. Consequently, $\Omega_m^{\rm grow}$ will be largely degenerate with any parameters that change the amplitude of the DES signal. In the case of the lensing information, which contributes significantly to the overall constraints, the amplitude is controlled by S_8, and is largely degenerate with the neutrino mass and intrinsic alignment parameters. Consequently, degeneracies between these parameters and $\Omega_m^{\rm grow}$ degrade the $\Omega_m^{\rm grow}$ contraints.

In fact, it is only when we combine two independent measures of structure growth, in the DES+Ext-all data combination, that we are able to fully constrain $\Omega_m^{\rm grow}$. For both DES+Ext-geo (where growth information comes only from DES) and Ext-all (where growth information comes only from BOSS RSD), we see that constraints on late-time structure growth are limited by our inability to break parameter degeneracies. The Ext-all measurements do not constrain $\Omega_m^{\rm grow}$ on their own because of a degeneracy between $\Omega_m^{\rm grow}$ and $\sum m_\nu$ (Fig. 6), while DES+Ext-geo is mainly limited by its inability to distinguish between $\Omega_m^{\rm grow}$ and $A_{\rm IA}$ (Fig. 17). When we combine all of these data together as DES+Ext-all, these degeneracies are broken and we are able to constrain $\Omega_m^{\rm grow}$. When we fix the sum of neutrino masses to 0.06 eV, we find that either Ext-all (with no DES data) or DES+Ext-geo are able to constrain both $\Omega_m^{\rm geo}$ and $\Omega_m^{\rm grow}$ on their own (Fig. 8).

When we split both Ω_m and w, a significant degeneracy between $\Omega_m^{\rm grow}$ and $w^{\rm grow}$ prevents us from being able to constrain the growth parameters even with DES+Ext-all data (Fig. 4). This suggests that additional growth probes would need to be included in order to provide enough redundancy to distinguish between Ω_m-like and w-like deviations from standard structure growth.

B. Are the data consistent with $\Theta^{\rm grow} = \Theta^{\rm geo}$?

Our constraints on $\Theta^{\rm grow}$ and $\Theta^{\rm geo}$ are statistically consistent, in the sense that we find tensions with ΛCDM to be less than 2σ when assessed using either the marginalized posterior for the difference $\Omega_m^{\rm grow} - \Omega_m^{\rm geo}$, or Bayesian Suspiciousness. For both the DES+Ext-geo and DES+Ext-all data combinations, the bulk of our posterior resides in the part of parameter space where $\Omega_m^{\rm grow} > \Omega_m^{\rm geo}$ (Fig. 5). This preference is not seen for DES data alone, where degeneracies with $A_{\rm s}$, and $A_{\rm IA}$ prevent one from placing a lower bound on the growth parameter (Fig. 10), shifting the posterior towards low $\Omega_m^{\rm grow}$. Equating the fraction of the posterior volume above the ΛCDM line of $\Omega_m^{\rm grow} = \Omega_m^{\rm geo}$ with equivalent one-sided p-values for a Gaussian distribution, we find that the DES-only posterior is in agreement with ΛCDM at the 0.5σ level, while DES+Ext-geo and DES+Ext-all are consistent with ΛCDM at 1.3σ and 1.6σ levels, respectively. Bayesian Suspiciousness quantifies the agreement of our posterior with $\Theta^{\rm grow} = \Theta^{\rm geo}$ in the model's full parameter space. According to this metric, when we split Ω_m the DES-only posterior has a 1.5σ tension with ΛCDM, DES+Ext-geo's tension is 1.9σ and DES+Ext-all's is 1.0σ. Fixing $\sum m_\nu = 0.06$ eV brings all three data combinations into $< 1\sigma$ agreement with ΛCDM. When we split both Ω_m and w we find a DES-only tension with wCDM of 1.6σ and a DES+Ext-all tension of 1.4σ. We caution that given the strong degeneracy between $\Omega_m^{\rm grow}$ and $A_{\rm IA}$, these results will be sensitive to changes in our model of the redshift dependence of intrinsic alignments (Fig. 13).

C. Is the DES preference for low σ_8 compared to Planck driven more by geometry or growth?

This question is not straightforward to answer, but our results support the idea that the S_8 tension is driven by constraints on the evolution of structure, as opposed to a mismatch between DES and Planck geometric constraints which somehow propagates into the S_8 parameter direction. To explain this conjecture, we note that for all data combinations we consider, constraints on geometry parameters are very similar to their un-split ΛCDM or wCDM constraints. This means that our split parameterization can be viewed as a generic way of allowing the properties of structure growth to vary around a fixed ΛCDM background. Thus, if splitting growth and geometry absorbs the offset between DES and Planck σ_8 measurements into a deviation from $\Omega_m^{\rm grow} = \Omega_m^{\rm geo}$, this would suggest that modifications to structure growth explain the σ_8 tension. The question therefore becomes: does our split parameterization relieve tension between DES and Planck?

The datasets we consider somewhat complicate this assessment because we do not analyze the full Planck likelihood that is typically used to quantify the S_8 tension. The closest comparison we can make is between DES and Ext-geo constraints. The Ext-geo data are less constraining than typical analyses of the full Planck likelihood with $A_{\rm Lens} = 1$, enough so that even in ΛCDM their 1σ confidence regions for σ_8 overlap substantially with those from DES. Since we construct the compressed Planck likelihood specifically to be insensitive to late-time structure growth (including by marginalizing over $A_{\rm Lens}$) this could be a clue that it is in fact growth-related CMB observ-

ables that drive the Planck preference for high σ_8 relative to DES.

That being said, our results may still contain some indication of the data properties which drive the σ_8 tension in ΛCDM. As we discuss in Sect. VI A, our DES+Ext-geo, Ext-all, and DES+Ext-all constraints on $\sum m_\nu$ depend sensitively on the relative value of A_s measured by Planck compared to S_8 measured by either DES or BOSS RSD (Fig. 7). Thus, the fact that those constraints favor high neutrino mass — and consequently, high $\Omega_m^{\rm grow}$— is possibly an indication that the CMB data prefer a higher density fluctuation amplitude than the LSS observables.

On the topic of tensions, we additionally note that splitting growth and geometry has almost no impact on H_0 constraints (Figs. 6, 17). This supports the idea that it is difficult to resolve the Hubble tension with simple model extensions to ΛCDM which alter late-time structure growth, echoing arguments made in Refs. [18, 132, 133], as well as findings from studies of decaying dark matter [21, 22, 134], modified gravity, and coupled dark energy models [53, 57].

D. Comparison to previous results

[NEW TEXT BEGINS HERE]

We now compare our results to those from other geometry-growth analyes in the literature. Direct comparisons are made challenging by the fact that each work made different choices in how to define the geometry-growth split, in addition to using different datasets and applying different modeling of the systematics. Nevertheless some general conclusions can nevertheless be drawn from these comparisons.

Our modeling choices are closest to those in Ref. [41]. They combine the CFHTLens weak lensing with an early-Universe prior based on Planck 2013 data (which is somewhat comparable to our DES+Ext-geo data combination which also has additional geometric constraints from supernovae and BAO), and also include galaxy cluster abundances which are sensitive to both geometry and growth. The fiducial analysis in Ref. [41] is however less conservative than ours as it fixes neutrino mass and does not include any intrisic alignments in the weak lensing modeling. As a result, even though Ref. [41] uses less constraining data, they constrain $\Omega_m^{\rm grow}$ more tightly than we do; the strength of our $\Omega_m^{\rm grow}$ constraints becomes comparable to theirs when we fix neutrino mass (see Appendix E 2). These differences aside, they agree with us in finding that $\Omega_m^{\rm geo}$ is better constrained than $\Omega_m^{\rm grow}$, that the constraints are compatible with $\Omega_m^{\rm grow} = \Omega_m^{\rm geo}$, and that the majority of the posterior resides in the $\Omega_m^{\rm grow} > \Omega_m^{\rm geo}$ part of parameter space. When splitting both w and Ω_m Ref. [41] finds a 3σ preference for $w^{\rm grow} > w^{\rm geo}$, strongly indicating less structure than would be expected given constraints from expansion history, though letting $\sum m_\nu$ vary entirely removes that tension in favor of high neutrino masses.

References [40] and [42] perform a "perturbations vs. background" split and use growth parameters to compute CMB anisotropy properties, rather than classifying growth parameters as specific to *late-time* structure evolution as done in this paper. Therefore the split-Ω_m model in these references probes different physics and is not directly comparable to our results. However, their results from splitting only w will be sensitive to only late-time growth-geometry discrepencies, and are more similar to what we study. In this split-w-only test, Refs. [40, 42] find consistency with wCDM. When Ref. [42] splits both Ω_m and w, they find $w^{\rm grow} > w^{\rm geo}$ at 3.5σ, in agreement with a similar analysis in Ref. [41], indicating less structure seen by growth observables than geometric ones. However because of the differences in the analyses, datasets, and treatment of the systematics, we caution against overinterpretation of that comparison.

[NEW TEXT ENDS HERE]

E. Outlook

The increasing precision of cosmological measurements will provide opportunities to perform more stringent tests of our standard cosmological model, including via future iterations of growth-geometry split analyses like the one presented here. In the coming months, updated Y3 galaxy clustering and weak lensing measurements will be released which have roughly three times the sky area, greater depth, and advances in methodology compared to Y1. Those measurements will provide improved constraints on both cosmological parameters and, crucially for testing growth-geometry consistency, the properties of intrinsic alignments.

It is worth noting that the external likelihoods in this paper were chosen to follow versions used in other DES Y1 papers [31], updated versions of both the Planck and BOSS likelihoods are already available and could be easily applied to near-future growth-geometry split studies. Relative to Planck 2015, the Planck 2018 cosmology results [57] have slight shifts in several parameters that would affect our compressed likelihood. Of these, the most impactful is that Planck 2018's improved polarization measurements lead to constraints on A_s which shift to lower values as they narrow by about a factor of two. As we saw in Fig. 7, even a small change in Planck's A_s constraints can have a significant impact on the region of overlap between CMB and late-time growth measurements in the $\sum m_\nu$-σ_8 plane. Lowering and tightening Planck's A_s constraint may be enough to shift Ext-all towards favoring low rather than high values of neutrino mass. This would in turn likely lower the values of $\Omega_m^{\rm grow}$ preferred by both DES+Ext-geo and DES+Ext-all.

One could also consider updating our BAO and RSD measurements to use the recently released eBOSS DR16 [61] measurements, which combine the DR12 BAO galaxies we use with the low-z Main Galaxy Sample (MGS) sample, high-z eBOSS galaxies (LRG and ELG),

high-z quasars, and Lyman-α forest mesurements. The high-z BAO measurements tend to prefer lower values of Ω_m and h than the galaxy samples used in DR12, so it is likely that switching to eBOSS would pull our constraints to slightly lower $\Omega_m^{\rm geo}$. However, as our analysis is currently more limited by its ability to constrain growth rather than geometry, the largest impact of switching from BOSS DR12 to eBOSS would be from the inclusion of additional RSD measurements, from the MGS, ELG, LRG, and QSO samples. Nearly all of these added samples have $f\sigma_8$ constraints that are high relative to the prediction from the Planck 2018 best-fit cosmology, so updating to eBOSS RSD would likely raise the σ_8 value preferred by Ext-all. Referencing Figs. 6 and 7, we predict that this would likely pull our DES+Ext-all results to lower $\Omega_m^{\rm grow}$ by making the Ext-all posterior more compatible with small neutrino mass.

Beyond increasing precision of individual measurements, including additional, complementary probes of structure growth could benefit future growth-geometry split analyses. We found in this analysis that including growth information from both DES and RSD allowed us to break degeneracies between $\Omega_m^{\rm grow}$, $\sum m_\nu$, and $A_{\rm IA}$ in order to more robustly test ΛCDM. Adding more observables that are sensitive to structure growth can help us further disentangle searches for deviations from ΛCDM from the effects of neutrino mass or astrophysical systematics. One approach to doing this could be to use full-shape information in the galaxy correlations measured by BOSS to directly constrain cosmological parameters, as in Refs [135–137]. Another, would be to include measurements of galaxy clusters. Previous growth-geometry split analyses in Refs. [41, 42] report that galaxy cluster number counts significantly influence their growth parameter constraints, though that is complicated by systematics related to the calibration of mass-observable relations. Thus, combining galaxy clustering and weak lensing data with galaxy cluster counts, as in Ref. [138], may be a powerful way to break degeneracies with systematics and add constraining power to future tests of growth-geometry consistency. Finally, another promising avenue could be to include CMB lensing data in a combined analysis like those in Refs. [131, 139]. Since the CMB lensing kernel reaches higher redshifts than galaxy lensing, this would give us a longer line-of-sight lever-arm for probing how LSS has evolved over time.

Looking further ahead, searching for deviations from the predictions of ΛCDM, particularly in the evolution of structure growth, will be a core part of future cosmological experiments, including DESI, the Rubin Observatory Legacy Survey of Space and Time, the Nancy Grace Roman Space Telescope, and Euclid, as well as the Simons Observatory and CMB S4. These searches may be conducted in a variety of ways, using parameterizations that range from purely phenomenological splits of data to more physical models derived from modified-gravity actions. Whatever the approach, some findings of this growth-geometry split analysis are broadly applicable: as measurements get more precise, it will only become more important to characterize how searches from beyond-ΛCDM physics are influenced by the assumptions about massive neutrinos and astrophysical systematics like intrinsic alignments, and a key way to distinguish between those things will be by performing combined analyses of multiple probes of structure growth.

ACKNOWLEDGMENTS

This paper has gone through internal review by the DES collaboration. JM has been supported by the Porat Fellowship at Stanford University, and by the Rackham Graduate School through a Predoctoral Fellowship.

The analysis made use of the software tools SciPy [140], NumPy [141], Matplotlib [142], CAMB [76, 77], GetDist [121], MultiNest [117–119], PolyChord [120], anesthetic [123], CosmoSIS [116], and Cosmolike [95]. It was supported through computational resources and services provided by the National Energy Research Scientific Computing Center (NERSC), a U.S. Department of Energy Office of Science User Facility operated under Contract No. DE-AC02-05CH11231; and by the Sherlock cluster, supported by Stanford University and the Stanford Research Computing Center.

Funding for the DES Projects has been provided by the U.S. Department of Energy, the U.S. National Science Foundation, the Ministry of Science and Education of Spain, the Science and Technology Facilities Council of the United Kingdom, the Higher Education Funding Council for England, the National Center for Supercomputing Applications at the University of Illinois at Urbana-Champaign, the Kavli Institute of Cosmological Physics at the University of Chicago, the Center for Cosmology and Astro-Particle Physics at the Ohio State University, the Mitchell Institute for Fundamental Physics and Astronomy at Texas A&M University, Financiadora de Estudos e Projetos, Fundação Carlos Chagas Filho de Amparo à Pesquisa do Estado do Rio de Janeiro, Conselho Nacional de Desenvolvimento Científico e Tecnológico and the Ministério da Ciência, Tecnologia e Inovação, the Deutsche Forschungsgemeinschaft and the Collaborating Institutions in the Dark Energy Survey.

The Collaborating Institutions are Argonne National Laboratory, the University of California at Santa Cruz, the University of Cambridge, Centro de Investigaciones Energéticas, Medioambientales y Tecnológicas-Madrid, the University of Chicago, University College London, the DES-Brazil Consortium, the University of Edinburgh, the Eidgenössische Technische Hochschule (ETH) Zürich, Fermi National Accelerator Laboratory, the University of Illinois at Urbana-Champaign, the Institut de Ciències de l'Espai (IEEC/CSIC), the Institut de Física d'Altes Energies, Lawrence Berkeley National Laboratory, the Ludwig-Maximilians Universität München and the associated Excellence Cluster Universe, the Univer-

sity of Michigan, NFS's NOIRLab, the University of Nottingham, The Ohio State University, the University of Pennsylvania, the University of Portsmouth, SLAC National Accelerator Laboratory, Stanford University, the University of Sussex, Texas A&M University, and the OzDES Membership Consortium.

Based in part on observations at Cerro Tololo Inter-American Observatory at NSF's NOIRLab (NOIRLab Prop. ID 2012B-0001; PI: J. Frieman), which is managed by the Association of Universities for Research in Astronomy (AURA) under a cooperative agreement with the National Science Foundation.

The DES data management system is supported by the National Science Foundation under Grant Numbers AST-1138766 and AST-1536171. The DES participants from Spanish institutions are partially supported by MICINN under grants ESP2017-89838, PGC2018-094773, PGC2018-102021, SEV-2016-0588, SEV-2016-0597, and MDM-2015-0509, some of which include ERDF funds from the European Union. IFAE is partially funded by the CERCA program of the Generalitat de Catalunya. Research leading to these results has received funding from the European Research Council under the European Union's Seventh Framework Program (FP7/2007-2013) including ERC grant agreements 240672, 291329, and 306478. We acknowledge support from the Brazilian Instituto Nacional de Ciência e Tecnologia (INCT) do e-Universo (CNPq grant 465376/2014-2).

This manuscript has been authored by Fermi Research Alliance, LLC under Contract No. DE-AC02-07CH11359 with the U.S. Department of Energy, Office of Science, Office of High Energy Physics.

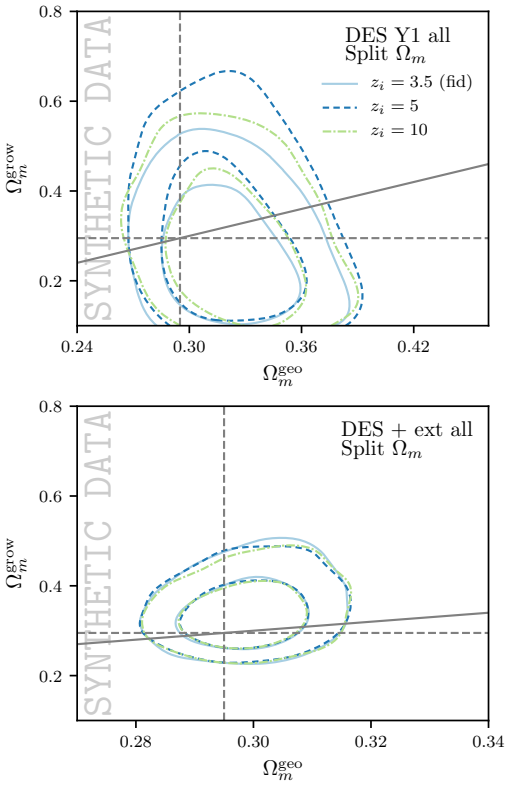

FIG. 9. The impact of changing the redshift z_i where growth parameters start controlling the evolution of the matter power spectrum, defined in Eq. (1), for DES-only (top panel) and DES+Ext-all (bottom panel). Countours show the 68% and 95% confidence regions from the analysis of synthetic data.

Appendix A: The impact of changing z_i

Here we characterize how our expected constraints depend on z_i, the redshift from Eq. (1) below which the evolution of the linear matter power spectrum is controlled by growth parameters. In addition to our fiducial choice of $z_i = 3.5$, we analyze the fiducial synthetic data vector with versions of our pipeline that have $z_i = 5$ and $z_i = 10$.

Fig. 9 shows the impact of these changes. For DES data alone we find that increasing z_i from 3.5 to 5 or 10 does slightly affect the upper bounds on $\Omega_m^{\rm grow}$, but does not significantly impact constraints on $\Omega_m^{\rm geo}$. In this simulated analysis we find that $z_i = 5$ results in the weakest $\Omega_m^{\rm grow}$ upper bound, while the bound from $z_i = 10$ is similar to but slightly weaker than the fiducial $z_i = 3.5$ result. The reason for the lack of monotonic trend in this is not clear, but given DES-only's poor constraining power on growth parameters and its sensitivity to projection effects and systematics (to be discussed in subsequent appendices), we refrain from over interpreting this. It is also possible that some of this variation is due to noise in the posterior estimate from Multinest, which can occur because of the small number of samples the posterior tails. Results from the joint analysis of DES+Ext-all are not significantly affected by changing z_i.

Appendix B: Evaluating projection effects

This Appendix discusses insights gained by studying the results of a simulated analysis in which we applied our parameter estimation pipeline to noiseless synthetic data generated by setting observables (e.g. BAO α parameters, weak lensing 2PCF) equal to theory predictions at fiducial parameter values. Specifically here we focus on the case where the synthetic data is generated using our baseline pipeline – that is, using the same modeling choices as in the theory predictions that we employ for for parameter estimation. Before analyzing real data, we used these simulated analyses to identify data and model combinations for which we expect marginalized posteriors to be reliably informative about whether growth and geometry constraints are consistent. This is not guaranteed: in high-dimensional parameter spaces like the one we consider, projecting the posterior volume onto one- or two-dimensional subspaces can result in offsets between the peaks of marginalized posteriors and the best fit parameter values. By comparing marginalized posteriors

from simulated analyses to the known input values, we are able to characterize the extent of these projection effects on our split parameters. We use this comparison to identify which data combinations will the focus of our analysis.

Our main results will be derived from the model and data combinations whose marginalized posteriors in simulated analyses are consistent with the input parameter values. These are:

- Split Ω_m constrained with DES+Ext-geo, and
- Split Ω_m constrained with DES+Ext-all.

For both of these model-data combinations, the input parameter values are contained within 68% confidence contour for the synthetic-data version of all two-dimensional constraint plots appearing in this paper. The input values also are within the 68% confidence interval of the one-dimensional marginalized posterior of the split parameter, as well as their differences.

We also consider two additional sets of constraints,

- Split Ω_m constrained by DES only, and
- Split Ω_m and w constrained by DES+Ext-all,

for which we find offsets between the input parameter values and the peaks of the marginalized 1D posteriors of the split parameters. In our simulated analysis, the DES-only marginalized posteriors for $\Omega_m^{\rm geo}$ and $\Omega_m^{\rm grow}$ are biased (high and low, respectively) relative to their input values by about 1σ. The DES+Ext-all constraints on split Ω_m and w exhibit $\sim 1\sigma$ offsets for marginalized posteriors of $\Omega_m^{\rm grow}$ and $w^{\rm grow}$. We therefore treat the results from these constraints with caution. Because we do not trust the one-dimensional posterior peaks to accurately reflect the best-fit values, we will not quote their one-dimensional marginalized parameter constraints. However, we will still report model-comparison measures and will show constraint contours for two-dimensional marginalized posteriors. This is motivated by the fact that in our simulated analyses the 68% confidence intervals of these two-dimensional marginalized posteriors do contain the input parameter values. Since simulated analysis results for DES+Ext-all, our most constraining dataset, results in constraints on split Ω_m and w that are offset from their input values, we do not consider constraints on the split w model from the less constraining data combinations, DES-only and DES+Ext-geo.

It can be instructive to examine the parameter degeneracies that drive the projection effects described above. The fact that the DES-only constraints on split Ω_m are biased high for $\Omega_m^{\rm geo}$ and low for $\Omega_m^{\rm grow}$ can be understood in terms of a degeneracy between $\Omega_m^{\rm grow}$ and $\Omega_m^{\rm geo}$, as well as degeneracies $\Omega_m^{\rm grow}$ has with the primordial power amplitude $A_{\rm s}$ and with the intrinsic alignment amplitude $A_{\rm IA}$. These degeneracies are illustrated (for real data) in Fig. 10. Focusing initially on the DES-only constraints, we note that very low $\Omega_m^{\rm grow}$ values are allowed because

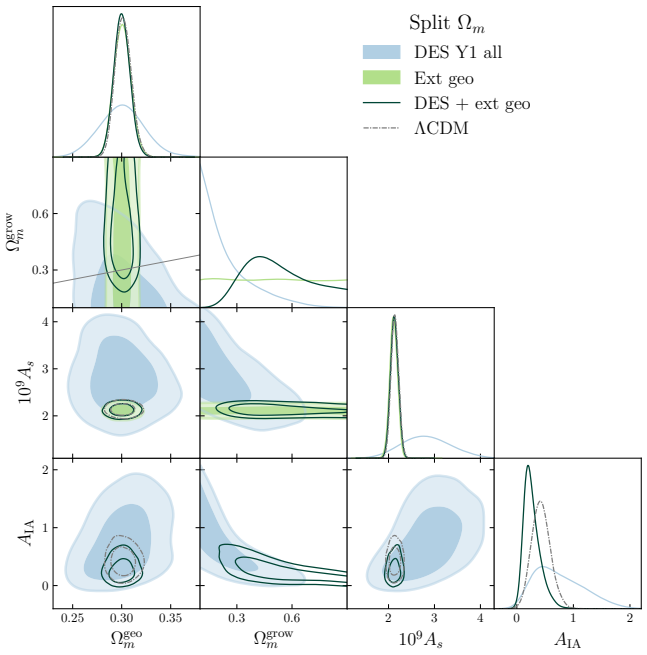

FIG. 10. Constraints illustrating the parameter degeneracies that are relevant to understanding the parameter space projection effects impacting the DES-only constraints on split Ω_m. Off diagonal panels show 68% and 95% confidence intervals, with DES-only results in blue, Ext-geo in light green, and DES+Ext-geo as the dark green unshaded contours. The gray diagonal line shows where $\Omega_m^{\rm grow} = \Omega_m^{\rm geo}$, and gray dashed contours show ΛCDM results for DES+Ext-geo.

they can be compensated by raising $A_{\rm s}$, while very high $\Omega_m^{\rm grow}$ values would presumably be ruled out based on the rate of structure growth occurring over the redshift range probed by DES. The degeneracy with $A_{\rm IA}$ occurs because intrinsic alignment contributions to the shear 2PCF appear in Eq. (6) via a factor $\propto A_{\rm IA}\Omega_m^{\rm grow}$. This causes the constant-posterior contours to have a banana-shape in the $\Omega_m^{\rm grow}$-$A_{\rm IA}$ plane, such that small values of $\Omega_m^{\rm grow}$ allow large values of $A_{\rm IA}$ and vice-versa. These degeneracies combine with the fact that the DES-only likelihood is relatively flat in $\Omega_m^{\rm grow}$ (as can be seen in the profile likelihood show in Fig. 16 below), to produce an offset in the projected posterior. This translates into an offset in $\Omega_m^{\rm geo}$ as well because there is a weak degeneracy between $\Omega_m^{\rm grow}$ and $\Omega_m^{\rm geo}$. The DES+Ext-geo and DES+Ext-all constraints do not show these offsets because the Planck constraints break the $\Omega_m^{\rm grow}$-$A_{\rm s}$ degeneracy.

The projection effects for DES+Ext-all constraints on split Ω_m and w are driven by the fact that the effects of $\Omega_m^{\rm grow}$ and $w^{\rm grow}$ on observables are very degenerate with one another (see Fig. 4). Though each of these growth parameters would have unbiased marginalized constraints if the other were fixed to its fiducial value, they are unconstrained when varied simultaneously. In other words, while the data we consider can constrain deviations from standard structure growth, it is not informative enough

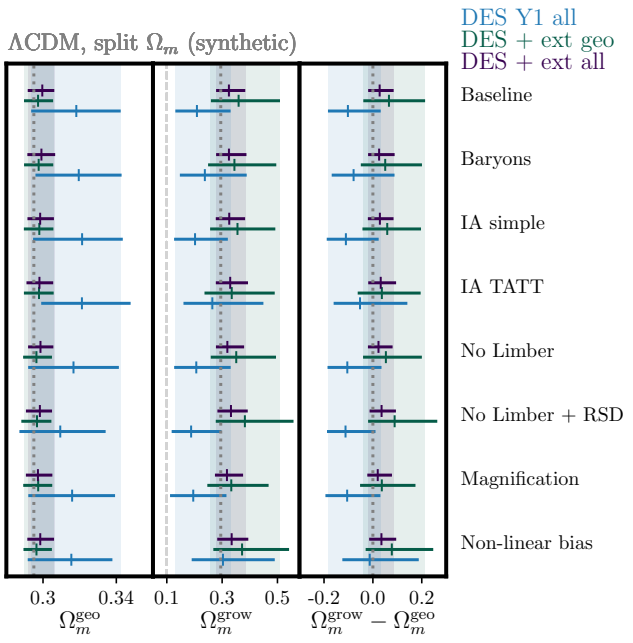

FIG. 11. Robustness of constraints to adding systematics to simulated data, for the split-Ω_m model. Data points and error bars represent the peak and 68% confidence intervals for marginalized one-dimensional posteriors. The vertical shaded regions correspond to the baseline error bars.

to distinguish between Ω_m-like and w-like changes.

Appendix C: Impact of unmodeled systematics

We additionally analyze synthetic data where the DES 3×2pt measurements are contaminated by unmodeled systematic effects in order to characterize our robustness against certain modeling assumptions. For example, we compute the 3×2pt observables using a non-linear galaxy bias model. By treating those synthetic observables as if they are data and fitting with our fiducial model (which assumes linear galaxy bias), we can quantify the extent to which unmodeled effects (here, the presence non-linear galaxy bias) biases our cosmological results. The synthetic data vectors we use in this study are the same as those used for similar tests in Refs. [95] and [31]. They are:

- Baseline - This data vector is equal to a theory prediction at a fiducial ΛCDM cosmology, using the same modeling choices as parameter estimation.

- Baryons - This data vector includes one case of possible effects of baryonic physics, the impact of AGN feedback on the non-linear power spectrum is included using the OWLS AGN hydrodynamical simulation [143], following the method described in [93].

- IA simple - Using the same nonlinear alignment model as in our fiducial model, this data vector is generated with $A_{\rm IA} = 0.5$ and $\eta_{IA} = 0.5$. We note that these parameters are marginalized over in our analysis, so including this data in our tests checks whether degeneracies between the intrinsic alignment parameters and the cosmological parameters can introduce biases.

- IA TATT - Here, the data vector is simulated with a different intrinsic alignment power spectrum shape. It is modeled by assuming all intrinsic alignments are generated by tidal torquing, which is quadratic in the tidal field, instead of the the linear tidal alignments described in our fiducial model. To compute it, we use the Tidal Alignment and Tidal Torquing model (TATT) [144] with tidal alignment amplitude $A_1 = 0$, tidal torquing amplitude $A_2 = 2$, and no z dependence.

- No Limber - This data vector has been simulated using a theory calculation done without the Limber approximation for $w(\theta)$.

- No Limber + RSD - This data vector has been simulated using a theory calculation done without the Limber approximation and including the contributions of redshift space distortions for $w(\theta)$ as described in [145]

- Magnification - This data vector is simulated including contribution from magnification to γ_t and $w(\theta)$, which are added in Fourier space as is described in [146].

- Non-linear bias - This data vector goes beyond our fiducial model of linear galaxy bias and models the relationship between matter δ and galaxy density fluctuations δ_g as [147, 148]

$$\delta_g = b_1^i \delta + \frac{1}{2} b_2^i [\delta^2 - \sigma^2] \tag{C1}$$

where σ is the variance in δ and i refers to the lens redshift bin. This theory data vector was computed using the FAST-PT code [149] with input values $b^i = \{1.45, 1.55, 1.65, 1.8, 2.0\}$ and the b_2 values used are estimated from fits to the Buzzard simulations [150] to be $b_2 = 0.412 - 2.143 b_1 + 0.929 b_1^2 + 0.008 b_1^3$.

More detailed descriptions of the generation of these data can be found in Refs. [95] and [31].

The metric for passing these tests is based on the one-dimensional marginalized posteriors for $\Omega_m^{\rm grow}$ and $\Omega_m^{\rm geo}$, as well the $w^{\rm grow}$ and $w^{\rm geo}$ for the parameterization where w is split. For each of the data combinations discussed above, we verify that the shift in the peak of the posterior is less than 0.3σ relative to the baseline analysis. We evaluate the size of these shifts by computing an effective σ by summing the two posteriors' asymmetric 68%

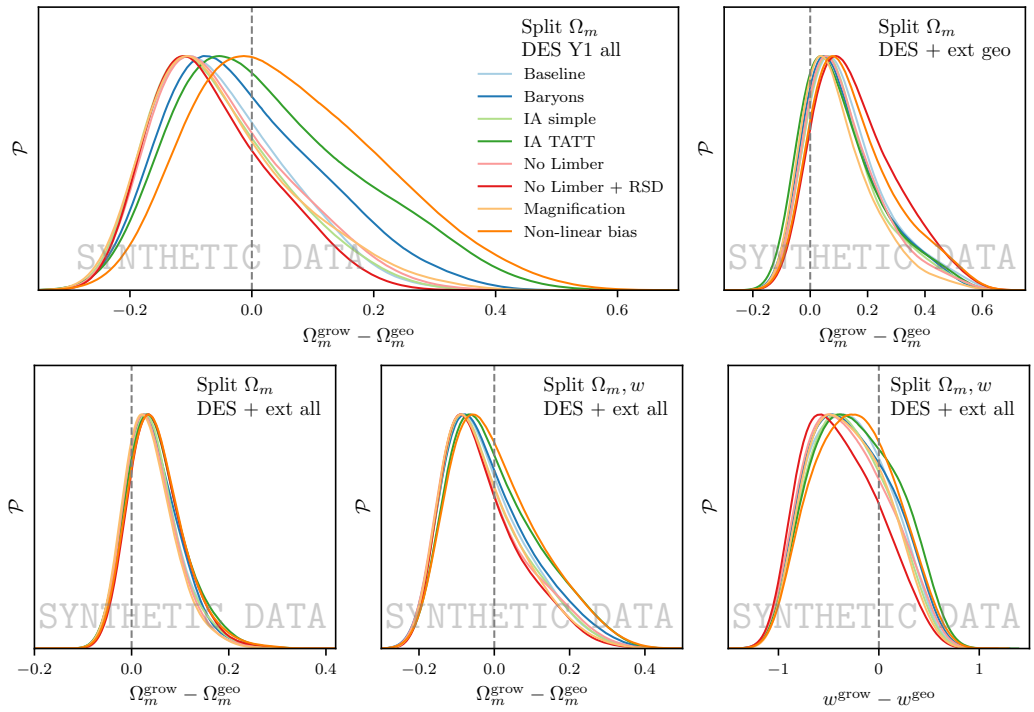

FIG. 12. Marginalized posteriors for synthetic data vectors contaminated by systematic effects, showing constraints on the difference between growth and geometry parameters. Top row: split-Ω_m results for DES-only (left) and for DES+Ext-geo (right). Bottom row: Results from DES+Ext-all when we split Ω_m (left), and when we split both Ω_m and w, showing growth-geometry differences for Ω_m (center) and w (right).

confidence intervals in quadrature. To state this more specifically, let $\hat{\theta}$ be the one-dimensional marginalized posterior peak on parameter θ, and suppose the baseline and contaminated constraints are labeled A and B such that $\hat{\theta}_A > \hat{\theta}_B$. Additionally let $\theta_A^{\texttt{low68}}$ be the lower bound of the 68% confidence interval for dataset A and $\theta_B^{\texttt{up68}}$ be the upper bound of the 68% confidence interval for dataset B. We quantify the size of the posterior shift as

$$\Delta_\theta = \frac{\hat{\theta}_A - \hat{\theta}_B}{\sqrt{(\hat{\theta}_a - \theta_A^{\texttt{low68}})^2 + (\theta_B^{\texttt{up68}} - \hat{\theta}_B)^2}}. \qquad \text{(C2)}$$

Summary plots showing the results for these tests are shown in Fig. 11 for split Ω_m and Fig. 14 for split Ω_m and w. We additionally show in Fig. 12 how the posteriors from these same synthetic-data analyses project onto the one-dimensional marginalized posteriors of the differences $\Omega_m^{\rm grow} - \Omega_m^{\rm geo}$ and $w^{\rm grow} - w^{\rm geo}$.

Both of the main model and data combinations identified in our fiducial simulated analysis of Appendix B (DES+Ext-geo and DES+Ext-all constraints on split Ω_m) pass these tests, as none of these changes result in a parameter shift larger than 0.3σ. For split Ω_m DES+Ext-geo results, the largest posterior shifts observed is in $\Omega_m^{\rm grow}$ and occurs when we add the effects of magnification to the synthetic data. The size of this shift is -0.16σ relative to the baseline simulated analysis. For DES+Ext-all, the systematic with the largest impact is non-linear galaxy bias, which shifts the $\Omega_m^{\rm grow}$ posterior by $+0.13\sigma$.

In addition to the prior volume effects described in Sect. B, the DES-only split Ω_m constraints and the DES+Ext-all constraints on split Ω_m and w should be treated with caution because they fail these tests, in the sense that the some of the systematics produced parameter shifts larger than our desired 0.3σ threshold. For the DES-only split-Ω_m results, this occurs for TATT intrinsic alignments, which changes the best-fit $\Omega_m^{\rm grow}$ by $+0.34\sigma$, and for nonlinear bias, which changes $\Omega_m^{\rm grow}$ by $+0.51\sigma$. All other shifts are below 0.3σ. For the DES+Ext-all constraints on split Ω_m and w the only systematic that generates a parameter shift larger than our threshold is the non-Limber and RSD modeling for galaxy clustering, which changes $w^{\rm grow}$ by -0.36σ.

Appendix D: Impact of changing analysis choices

Before revealing the non-offset (unblinded) parameter estimates, we test the robustness of our analysis of real data against changes to various analysis choices. We perform this test similarly to the systematics tests described in Appendix C, but instead of analyzing contaminated synthetic data, we compare parameter estimates obtained by running on the same real data, but alter-

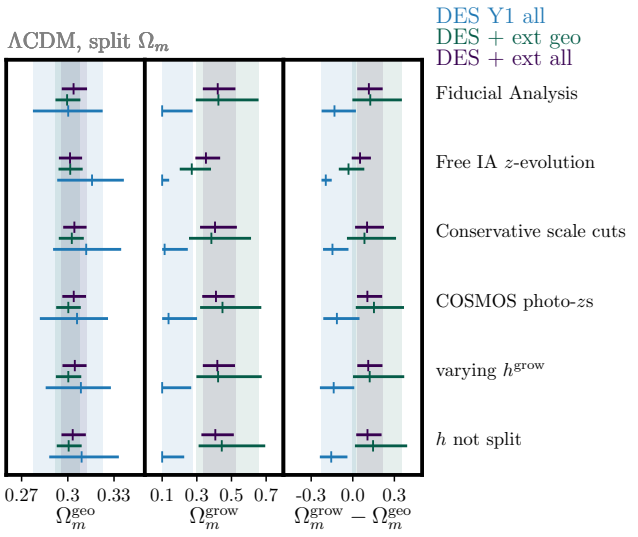

FIG. 13. Robustness of real-data constraints to changes in analysis choices when we split Ω_m. Data points and error bars represent the peak and 68% confidence intervals for marginalized one-dimensional posteriors. The vertical shaded regions correspond to the 68% confidence interval of the baseline measurements.

ing aspects of our analysis pipeline. These changes are, following the analysis in Ref. [31]:

- Free IA z-evolution - Instead of assuming that the intrinsic alignment amplitude scales as a power law in redshift, we allow its amplitude to vary for independently for each source redshift bin.
- Conservative scale cuts - We restrict our analysis to DES 2PCF measurements to large angles which are insensitive to non-linear LSS modeling.
- COSMOS photo-z's - We use alternative photometric redshifts for the DES source galaxies, obtained by resampling COSMOS data following the procedure in [90].

Additionally, for the split Ω_m model we also show the results of additional tests examining the impact of changing the treatment of the Hubble parameter in our split parameterization. Recalling our fiducial analysis splits h and fixes $h^{\rm grow} = 0.6881$, we show how parameter constraints change for:

- Varying $h^{\rm grow}$ - We allow $h^{\rm grow}$ to vary over the same $[0.1, 0.9]$ prior range as $h \equiv h^{\rm geo}$.
- h not split - We require $h^{\rm grow} = h^{\rm geo}$ and vary it as in ΛCDM.

These h tests were conducted after the true analysis results were revealed (after unblinding).

The results of these tests are summarized in Fig. 13 for the split Ω_m analysis, and in Fig. 15 for split Ω_m and w. We quantify the changes from the baseline analysis following the same method as in Appendix C above.

Notably, for all data and model combinations we see significant parameter shifts in growth parameter estimates when we allow the intrinsic alignment amplitude to vary independently in each redshift bin. For all pipeline variations other than free IA z-evolution, we find that our main results, DES+Ext-geo and DES+Ext-all constraints on split Ω_m, are robust. For DES+Ext-geo, the largest parameter shift relative to the baseline analysis is a $+0.25\sigma$ change in $\Omega_m^{\rm geo}$, which occurs when we switch to conservative scale cuts. For DES+Ext-all, the conservative scale cuts and not splitting h tie for the largest shift, a -0.10σ change in $\Omega_m^{\rm grow}$.

The DES-only split Ω_m results and the DES+Ext-all results for split Ω_m and w are less robust, even setting the free IA z-evolution results aside. For the DES-only constraints on split Ω_m, conservative scale cuts produce a 0.38σ shift in $\Omega_m^{\rm geo}$, while all other parameter shifts are below 0.3σ. For DES+Ext-all constraints on split Ω_m and w, using conservative scale cuts moves $\Omega_m^{\rm grow}$ by 0.31σ shift and $w^{\rm grow}$ by $+0.59\sigma$, and using the COSMOS photo-zs causes $w^{\rm grow}$ to change by 0.36σ.

After observing this behavior in parameter-offset (blinded) results from real data, we performed an analysis of synthetic data using the binned-IA model in order to better characterize its impact, and found that free IA z evolution produced a similar change in posteriors. We hypothesize that the large parameter shifts, especially in $\Omega_m^{\rm grow}$, occurs when we introduce more freedom in IA redshift evolution because of a parameter-space projection effect. As discussed for our fiducial NLA IA model in Appendix B, the fact that $\Omega_m^{\rm grow}$ is poorly constrained and degenerate with $A_{\rm IA}$ causes the DES-only posterior to be skewed towards low $\Omega_m^{\rm grow}$ values. When we allow the IA amplitude to vary independently for each source redshift bin, this opens a large volume of parameter space where small $\Omega_m^{\rm grow}$ can compensate large IA amplitudes. That low-$\Omega_m^{\rm grow}$ posterior volume is much larger than the allowed region of parameter space where $\Omega_m^{\rm grow}$ is high but all four IA amplitudes are small. This means that in the absence of strong constraints on $\Omega_m^{\rm grow}$, small $\Omega_m^{\rm grow}$ values will dominate one- or two-dimensional projections of the posterior. Degeneracies between $\Omega_m^{\rm grow}$ and other parameters will propagate that effect to other parameters like $\Omega_m^{\rm geo}$. This is perhaps analogous to Ref. [130]'s finding that opening up "too much" freedom in the IA model causes S_8 constraints to shift to smaller values, and we posit that it is why opening up additional IA parameter space causes such dramatic parameter shifts in Figs. 13 and 15.

To support this hypothesis, in Fig. 16 we show the profile likelihood for $\Omega_m^{\rm grow}$ for DES-only and DES+Ext-all constraints on synthetic data. The vertical axes of these plots show the maximum likelihood in our chain samples which have $\Omega_m^{\rm grow}$ within a narrow bin. These profiles are noisy and exhibit sharp drop-offs because our sampler (Multinest in this case) returned very few chain sam-

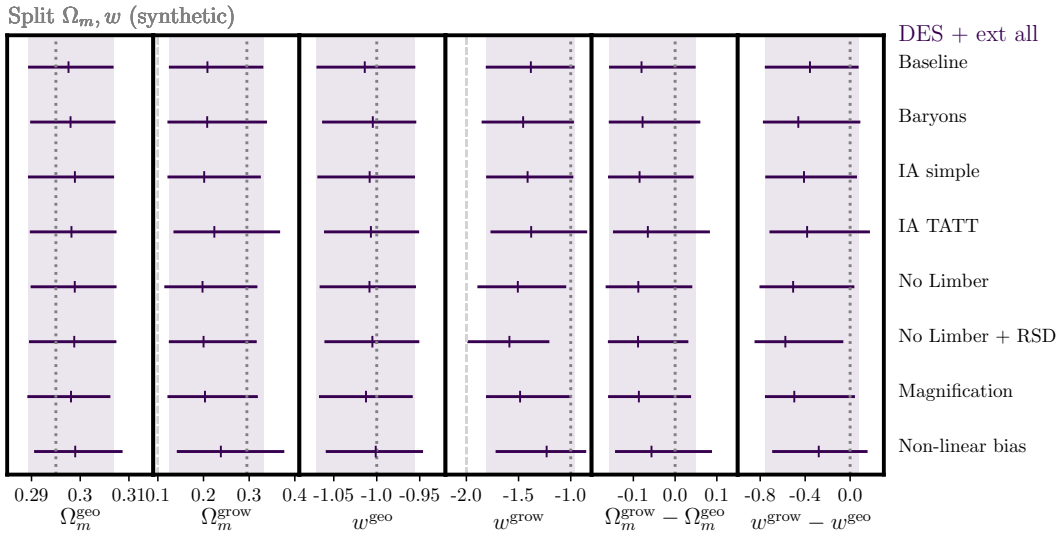

FIG. 14. Robustness of results to adding systematics to simulated data for the model splitting Ω_m and w. Data points and error bars represent the peak and 68% confidence intervals for marginalized one-dimensional posteriors. The vertical shaded regions correspond to the baseline error bars.

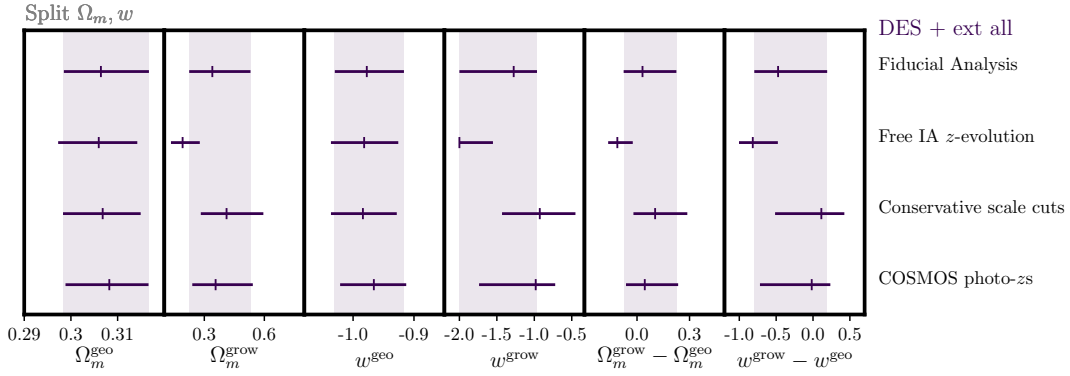

FIG. 15. Robustness of real-data constraints to changes in analysis choices when we split Ω_m and w. Data points and error bars represent the peak and 68% confidence intervals for marginalized one-dimensional posteriors. The vertical shaded regions correspond to the 68% confidence interval of the baseline measurements.

ples in that region of parameter space. Where there are enough samples to compare the baseline and binned-IA profiles, we see that they have very similar profile likelihoods. This means that the "free IA z-evolution" model does not actually produce an improved fit to the data at small Ω_m compared to our fiducial model. Rather, the posterior peaks at smaller $\Omega_m^{\rm grow}$ because binning IA increases the relative volume of the parameter space, and thus the density of chain samples, associated with small $\Omega_m^{\rm grow}$ compared to high $\Omega_m^{\rm grow}$. In other words, the change in posterior peak comes from parameter volume projection effects.

Current data [4, 130, 131] are not able to rule out models with this much variation in the IA amplitude, but neither do they provide evidence for IA redshift evolution beyond our NLA power law, nor is there a strong theoretical motivation for it. Given this, we proceed with our analysis despite the nominal failure of this robustness test.

Appendix E: Additional results

1. Parameter degeneracies without RSD data

We include Fig. 17 to supplement the discussion in Sect. VI about how splitting Ω_m impacts constraint on $\sum m_\nu$, S_8, h and $A_{\rm IA}$. It is identical to Fig. 6, except in that it does not include BOSS RSD measurements. The off-diagonal panels show the 68% and 95% confidence intervals for DES-only as blue shaded regions (identical to those in Fig. 6), for Ext-geo in light green shaded re-

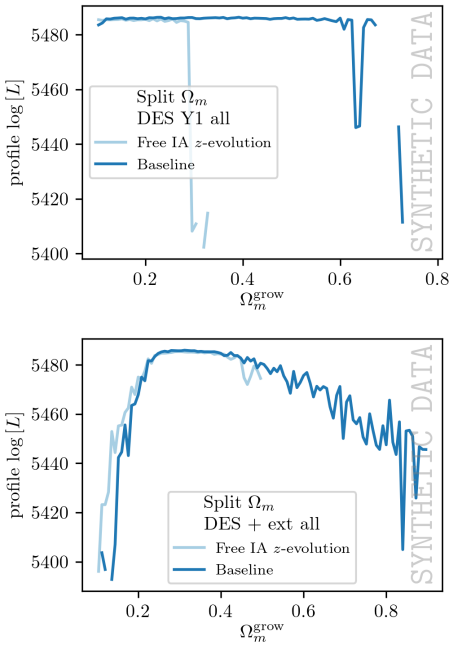

FIG. 16. Likelihood profile showing the maximum likelihood for chain samples within narrow bins of $\Omega_m^{\rm grow}$. The sharp step functions in the DES-only plot shows where the sample density decreases significantly due to the $A_{\rm IA}$-$\Omega_m^{\rm grow}$ projection effects discussed in Appendix B.

gions, and for the DES+Ext-geo combination as dark green unshaded contours. Diagonal gray lines denote where $\Omega_m^{\rm grow} = \Omega_m^{\rm geo}$, and gray dashed contours show ΛCDM results for DES+Ext-geo. The diagonal panels show normalized marginalized posteriors for individual parameters.

2. Impact of fixing $\sum m_\nu$

Here we present additional information about the impact of fixing neutrino mass to supplement the discussion and Fig. 8 in Sect. VI A. Table IV reports tension and model comparison metrics for the fixed neutrino mass analyses. It follows the same notation and conventions as what is used for the main results in Table III.

Additionally, Fig. 18 shows how the Ext-all constraints change when we either fix $\sum m_\nu$ to its minimum allowed value or we revert to ΛCDM with $\Omega_m^{\rm grow} = \Omega_m^{\rm geo}$. In that Figure the shaded pink contours, which are the same as those in Fig. 6, show our baseline DES+Ext-all constraints when Ω_m is split and the sum of neutrino masses is varied. The solid red contours show how these constraints change when we fix $\sum m_\nu = 0.06\,\text{eV}$, while the solid gray contours show what happens when we switch to ΛCDM (but still vary neutrino mass). The dashed black lines show what happens when we both require $\Omega_m^{\rm grow} = \Omega_m^{\rm geo}$ and fix $\sum m_\nu$.

[1] Dark Energy Survey Collaboration (DES), Phys. Rev. Lett. **122**, 171301 (2019), arXiv:1811.02375 [astro-ph.CO].
[2] A. Joyce, B. Jain, J. Khoury, and M. Trodden, Phys. Rept. **568**, 1 (2015), arXiv:1407.0059 [astro-ph.CO].
[3] D. H. Weinberg, M. J. Mortonson, D. J. Eisenstein, C. Hirata, A. G. Riess, and E. Rozo, Phys. Rept. **530**, 87 (2013), arXiv:1201.2434 [astro-ph.CO].
[4] Dark Energy Survey Collaboration (DES), Phys. Rev. **D98**, 043526 (2018), arXiv:1708.01530 [astro-ph.CO].
[5] W. Handley and P. Lemos, Phys. Rev. **D100**, 043504 (2019), arXiv:1902.04029 [astro-ph.CO].
[6] H. Hildebrandt *et al.*, Mon. Not. Roy. Astron. Soc. **465**, 1454 (2017), arXiv:1606.05338 [astro-ph.CO].
[7] S. Joudaki *et al.*, Mon. Not. Roy. Astron. Soc. **465**, 2033 (2017), arXiv:1601.05786 [astro-ph.CO].
[8] S. Joudaki, M. Kaplinghat, R. Keeley, and D. Kirkby, Phys. Rev. D **97**, 123501 (2018), arXiv:1710.04236 [astro-ph.CO].
[9] A. Leauthaud *et al.*, Mon. Not. Roy. Astron. Soc. **467**, 3024 (2017), arXiv:1611.08606 [astro-ph.CO].
[10] E. van Uitert *et al.*, Mon. Not. Roy. Astron. Soc. **476**, 4662 (2018), arXiv:1706.05004 [astro-ph.CO].
[11] S. Joudaki *et al.*, Mon. Not. Roy. Astron. Soc. **474**, 4894 (2018), arXiv:1707.06627 [astro-ph.CO].
[12] C. Hikage *et al.* (HSC), Publ. Astron. Soc. Jap. **71**, Publications of the Astronomical Society of Japan, Volume 71, Issue 2, April 2019, 43, https://doi.org/10.1093/pasj/psz010 (2019), arXiv:1809.09148 [astro-ph.CO].
[13] T. Hamana *et al.*, Publ. Astron. Soc. Jap. **72**, Publications of the Astronomical Society of Japan, Volume 72, Issue 1, February 2020, 16, https://doi.org/10.1093/pasj/psz138 (2020), arXiv:1906.06041 [astro-ph.CO].
[14] C. Heymans *et al.* (KiDS), arXiv:2007.15632 (2020), arXiv:2007.15632 [astro-ph.CO].
[15] Y. Park and E. Rozo, arXiv:1907.05798 (2019), arXiv:1907.05798 [astro-ph.CO].
[16] A. G. Riess *et al.*, Astrophys. J. **826**, 56 (2016), arXiv:1604.01424 [astro-ph.CO].
[17] A. G. Riess, S. Casertano, W. Yuan, L. M. Macri, and D. Scolnic, Astrophys. J. **876**, 85 (2019), arXiv:1903.07603 [astro-ph.CO].
[18] L. Knox and M. Millea, Phys. Rev. D **101**, 043533 (2020), arXiv:1908.03663 [astro-ph.CO].
[19] J. C. Hill, E. McDonough, M. W. Toomey, and S. Alexander, Phys. Rev. D **102**, 043507 (2020), arXiv:2003.07355 [astro-ph.CO].
[20] E. Di Valentino, C. Bøehm, E. Hivon, and F. R. Bouchet, Phys. Rev. D **97**, 043513 (2018), arXiv:1710.02559 [astro-ph.CO].
[21] S. J. Clark, K. Vattis, and S. M. Koushiappas, arXiv:2006.03678 (2020), arXiv:2006.03678 [astro-

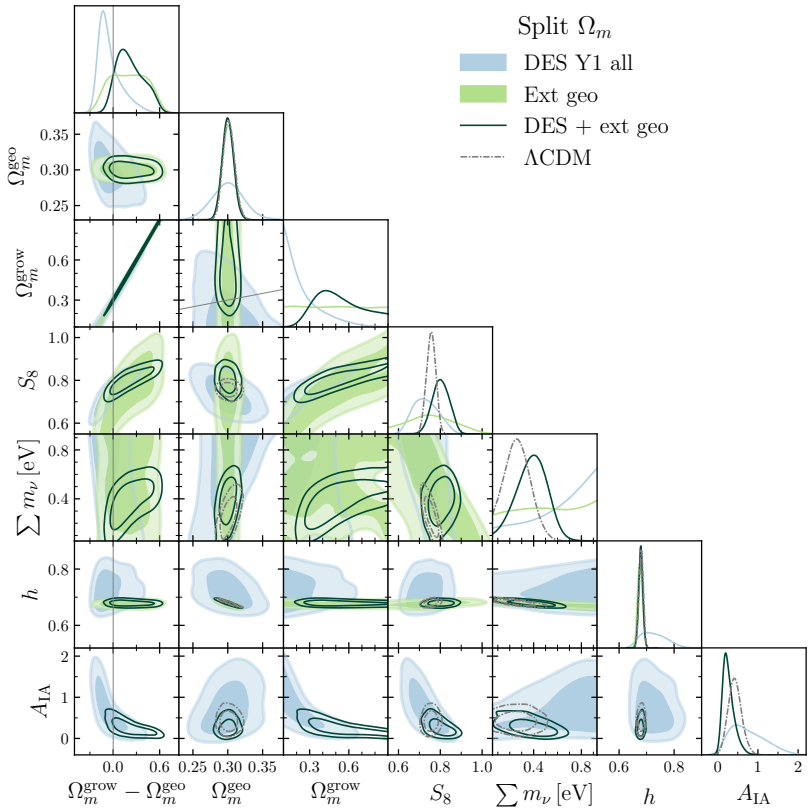

FIG. 17. Marginalized constraints from DES and Ext-geo data. This plot is identical to Fig. 6, but uses the external dataset that does not include BOSS RSD.

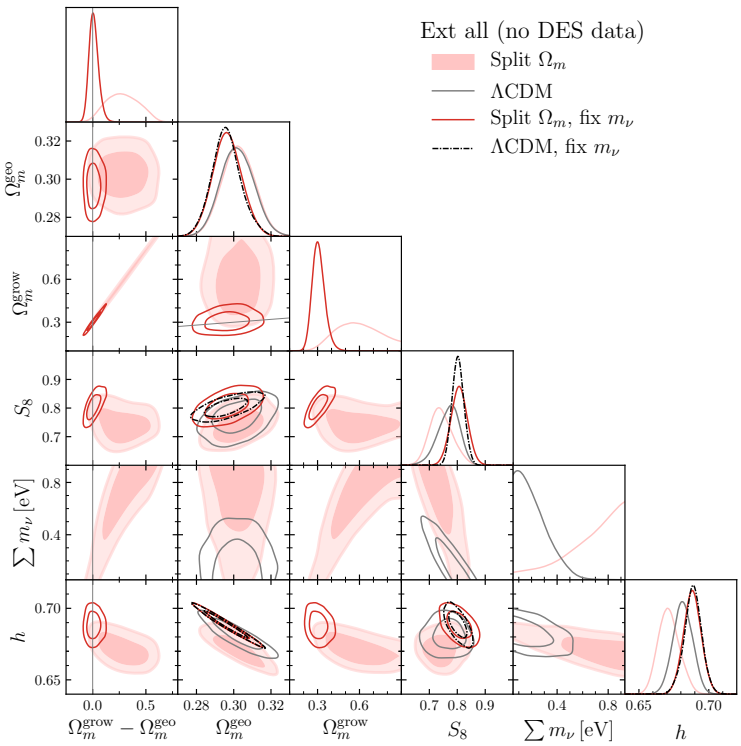

FIG. 18. Ext-all constraints (not including any DES information) showing the effect of fixing neutrino mass for both the split Ω_m parameterization and ΛCDM.

TABLE IV. Constraints, tension, and model comparison statistics for split parameters when we fix $\sum m_\nu = 0.06$ eV.

ΛCDM, fix m_ν	DES	DES+Ext-geo	DES+Ext-all
Ω_m	$0.279^{+0.023}_{-0.017}$	$0.289^{+0.007}_{-0.005}$	$0.290^{+0.007}_{-0.006}$
$\tilde{d}$	13.4 ± 0.7	15.7 ± 0.7	16.1 ± 0.7
$\log S^{\rm dat}$	-	-0.7 ± 0.2	-1.1 ± 0.2
$p(S > S^{\rm dat})$	-	0.23 ± 0.05	0.15 ± 0.05
equiv. σ	-	1.2 ± 0.1	1.4 ± 0.2

Split Ω_m, fix m_ν	DES	DES+Ext-geo	DES+Ext-all
$\Omega_m^{\rm grow} - \Omega_m^{\rm geo}$	-	$-0.040^{+0.074}_{-0.055}$	$-0.007^{+0.036}_{-0.037}$
$\Omega_m^{\rm geo}$	-	$0.291^{+0.007}_{-0.007}$	$0.292^{+0.006}_{-0.006}$
$\Omega_m^{\rm grow}$	-	$0.252^{+0.070}_{-0.051}$	$0.284^{+0.036}_{-0.035}$
$\tilde{d}$	14.5 ± 0.7	17.6 ± 0.9	16.8 ± 0.8
$\log S^{\rm dat}$	-	-1.2 ± 0.3	-0.5 ± 0.3
$p(S > S^{\rm dat})$	-	0.11 ± 0.06	0.29 ± 0.06
equiv. σ	-	1.6 ± 0.3	1.1 ± 0.1
$\log S^{\rm mod}$	0.0 ± 0.2	0.4 ± 0.2	0.0 ± 0.2
$p(S > S^{\rm mod})$	0.45 ± 0.24	0.57 ± 0.20	0.39 ± 0.23
equiv. σ	0.8 ± 0.4	0.5 ± 0.3	0.9 ± 0.4

ph.CO].
[22] A. Chen *et al.* (DES), arXiv:2011.04606 (2020), arXiv:2011.04606 [astro-ph.CO].
[23] S. Aiola *et al.* (ACT), arXiv:2007.07288 (2020), arXiv:2007.07288 [astro-ph.CO].
[24] DES and SPT Collaborations, Phys. Rev. D **100**, 023541 (2019), arXiv:1810.02322 [astro-ph.CO].
[25] F. Bianchini *et al.* (SPT), Astrophys. J. **888**, 119 (2020), arXiv:1910.07157 [astro-ph.CO].
[26] M. Ishak, A. Upadhye, and D. N. Spergel, Phys. Rev. **D74**, 043513 (2006), arXiv:astro-ph/0507184 [astro-ph].
[27] E. V. Linder, Phys. Rev. **D72**, 043529 (2005), arXiv:astro-ph/0507263 [astro-ph].
[28] L. Knox, Y.-S. Song, and J. A. Tyson, Phys. Rev. **D74**, 023512 (2006), arXiv:astro-ph/0503644 [astro-ph].
[29] E. Bertschinger, Astrophys. J. **648**, 797 (2006), arXiv:astro-ph/0604485 [astro-ph].
[30] D. Huterer and E. V. Linder, Phys. Rev. **D75**, 023519 (2007), arXiv:astro-ph/0608681 [astro-ph].
[31] Dark Energy Survey Collaboration (DES), Phys. Rev. **D99**, 123505 (2019), arXiv:1810.02499 [astro-ph.CO].
[32] Dark Energy Survey Collaboration (DES), Mon. Not. Roy. Astron. Soc. **483**, 4866 (2019), arXiv:1712.06209 [astro-ph.CO].
[33] Dark Energy Survey Collaboration (DES), Phys. Rev. D **102**, 023509 (2020), arXiv:2002.11124 [astro-ph.CO].
[34] Dark Energy Survey Collaboration (DES), Astrophys. J. **872**, L30 (2019), arXiv:1811.02374 [astro-ph.CO].
[35] K. N. Abazajian and S. Dodelson, Phys. Rev. Lett. **91**, 041301 (2003), arXiv:astro-ph/0212216 [astro-ph].
[36] B. Jain and A. Taylor, Phys. Rev. Lett. **91**, 141302 (2003), arXiv:astro-ph/0306046 [astro-ph].
[37] J. Zhang, L. Hui, and A. Stebbins, Astrophys. J. **635**, 806 (2005), arXiv:astro-ph/0312348 [astro-ph].
[38] F. Simpson and S. Bridle, Phys. Rev. **D71**, 083501 (2005), arXiv:astro-ph/0411673 [astro-ph].
[39] H. Zhan, L. Knox, and J. A. Tyson, Astrophys. J. **690**, 923 (2009), arXiv:0806.0937 [astro-ph].
[40] S. Wang, L. Hui, M. May, and Z. Haiman, Phys. Rev. **D76**, 063503 (2007), arXiv:0705.0165 [astro-ph].
[41] E. J. Ruiz and D. Huterer, Phys. Rev. **D91**, 063009 (2015), arXiv:1410.5832 [astro-ph.CO].
[42] J. L. Bernal, L. Verde, and A. J. Cuesta, JCAP **1602**, 059 (2016), arXiv:1511.03049 [astro-ph.CO].
[43] W. Lin and M. Ishak, Phys. Rev. **D96**, 023532 (2017), arXiv:1705.05303 [astro-ph.CO].
[44] P. Zhang, M. Liguori, R. Bean, and S. Dodelson, Phys. Rev. Lett. **99**, 141302 (2007), arXiv:0704.1932 [astro-ph].
[45] L. Amendola, M. Kunz, M. Motta, I. D. Saltas, and I. Sawicki, Phys. Rev. **D87**, 023501 (2013), arXiv:1210.0439 [astro-ph.CO].
[46] A. Abate and O. Lahav, Mon. Not. Roy. Astron. Soc. **389**, 47 (2008), arXiv:0805.3160 [astro-ph].
[47] M. Chu and L. Knox, Astrophys. J. **620**, 1 (2005), arXiv:astro-ph/0407198 [astro-ph].
[48] J. M. Z. Matilla, Z. Haiman, A. Petri, and T. Namikawa, Phys. Rev. **D96**, 023513 (2017), arXiv:1706.05133 [astro-ph.CO].
[49] S. Alam *et al.* (BOSS), Mon. Not. Roy. Astron. Soc. **470**, 2617 (2017), arXiv:1607.03155 [astro-ph.CO].
[50] S. Basilakos and F. K. Anagnostopoulos, Eur. Phys. J. C **80**, 212 (2020), arXiv:1903.10758 [astro-ph.CO].
[51] A. Ferté, D. Kirk, A. R. Liddle, and J. Zuntz, Phys. Rev. **D99**, 083512 (2019), arXiv:1712.01846 [astro-ph.CO].
[52] F. Simpson *et al.*, Mon. Not. Roy. Astron. Soc. **429**, 2249 (2013), arXiv:1212.3339 [astro-ph.CO].
[53] P. A. R. Ade *et al.* (Planck), Astron. Astrophys. **594**, A14 (2016), arXiv:1502.01590 [astro-ph.CO].
[54] S. Joudaki *et al.*, Mon. Not. Roy. Astron. Soc. **471**, 1259 (2017), arXiv:1610.04606 [astro-ph.CO].
[55] C. Garcia-Quintero and M. Ishak, arXiv:2009.01189 (2020), arXiv:2009.01189 [astro-ph.CO].
[56] E. V. Linder, JCAP **10**, 042 (2020), arXiv:2003.10453 [astro-ph.CO].
[57] N. Aghanim *et al.* (Planck), Astron. Astrophys. **641**, A6 (2020), arXiv:1807.06209 [astro-ph.CO].
[58] M. Ata *et al.*, Mon. Not. Roy. Astron. Soc. **473**, 4773 (2018), arXiv:1705.06373 [astro-ph.CO].
[59] V. de Sainte Agathe *et al.*, Astron. Astrophys. **629**, A85 (2019), arXiv:1904.03400 [astro-ph.CO].
[60] M. Blomqvist *et al.*, Astron. Astrophys. **629**, A86 (2019), arXiv:1904.03430 [astro-ph.CO].
[61] S. Alam *et al.* (eBOSS), arXiv:2007.08991 (2020), arXiv:2007.08991 [astro-ph.CO].
[62] E. Krause, T. Eifler, *et al.* (DES), Submitted to: Phys. Rev. D (2017), arXiv:1706.09359 [astro-ph.CO].
[63] R. E. Smith, J. A. Peacock, A. Jenkins, S. D. M. White, C. S. Frenk, F. R. Pearce, P. A. Thomas, G. Efstathiou, and H. M. P. Couchmann (VIRGO Consortium), Mon. Not. Roy. Astron. Soc. **341**, 1311 (2003), arXiv:astro-ph/0207664 [astro-ph].
[64] S. Bird, M. Viel, and M. G. Haehnelt, Mon. Not. Roy.

Astron. Soc. **420**, 2551 (2012), arXiv:1109.4416 [astro-ph.CO].
[65] R. Takahashi, M. Sato, T. Nishimichi, A. Taruya, and M. Oguri, Astrophys. J. **761**, 152 (2012), arXiv:1208.2701 [astro-ph.CO].
[66] D. N. Limber, Astrophys. J. **117**, 134 (1953).
[67] M. LoVerde and N. Afshordi, Phys. Rev. D **78**, 123506 (2008), arXiv:0809.5112 [astro-ph].
[68] S. Bridle and L. King, New J. Phys. **9**, 444 (2007), arXiv:0705.0166 [astro-ph].
[69] M. Kilbinger *et al.*, Astron. Astrophys. **497**, 677 (2009), arXiv:0810.5129 [astro-ph].
[70] P. A. R. Ade *et al.* (Planck), Astron. Astrophys. **594**, A13 (2016), arXiv:1502.01589 [astro-ph.CO].
[71] D. Brout *et al.* (DES), Astrophys. J. **874**, 150 (2019), arXiv:1811.02377 [astro-ph.CO].
[72] D. M. Scolnic *et al.*, Astrophys. J. **859**, 101 (2018), arXiv:1710.00845 [astro-ph.CO].
[73] J. Marriner, J. Bernstein, R. Kessler, H. Lampeitl, R. Miquel, J. Mosher, R. C. Nichol, M. Sako, and M. Smith (SDSS), Astrophys. J. **740**, 72 (2011), arXiv:1107.4631 [astro-ph.CO].
[74] R. Kessler and D. Scolnic, Astrophys. J. **836**, 56 (2017), arXiv:1610.04677 [astro-ph.CO].
[75] G. Efstathiou and J. R. Bond, Mon. Not. Roy. Astron. Soc. **304**, 75 (1999), arXiv:astro-ph/9807103 [astro-ph].
[76] A. Lewis, A. Challinor, and A. Lasenby, Astrophys. J. **538**, 473 (2000), arXiv:astro-ph/9911177 [astro-ph].
[77] C. Howlett, A. Lewis, A. Hall, and A. Challinor, JCAP **1204**, 027 (2012), arXiv:1201.3654 [astro-ph.CO].
[78] J. A. Frieman, D. Huterer, E. V. Linder, and M. S. Turner, Phys. Rev. **D67**, 083505 (2003), arXiv:astro-ph/0208100 [astro-ph].
[79] A. Drlica-Wagner *et al.* (DES), Astrophys. J. Suppl. **235**, 33 (2018), arXiv:1708.01531 [astro-ph.CO].
[80] B. Flaugher, H. T. Diehl, *et al.* (DES), Astron. J. **150**, 150 (2015), arXiv:1504.02900 [astro-ph.IM].
[81] S. Desai *et al.* (BCS), Astrophys. J. **757**, 83 (2012), arXiv:1204.1210 [astro-ph.CO].
[82] I. Sevilla *et al.* (DES), in *Particles and fields. Proceedings, Meeting of the Division of the American Physical Society, DPF 2011, Providence, USA, August 9-13, 2011* (2011) arXiv:1109.6741 [astro-ph.IM].
[83] J. J. Mohr *et al.* (DES), *Proceedings, Advanced Optical and Mechanical Technologies in Telescopes and Instrumentation: Marseille, France, June 23-28, 2008*, Proc. SPIE Int. Soc. Opt. Eng. **7016**, 70160L (2008), arXiv:0807.2515 [astro-ph].
[84] E. Morganson *et al.* (DES), Publ. Astron. Soc. Pac. **130**, 074501 (2018), arXiv:1801.03177 [astro-ph.IM].
[85] E. Rozo *et al.* (DES), Mon. Not. Roy. Astron. Soc. **461**, 1431 (2016), arXiv:1507.05460 [astro-ph.IM].
[86] E. Huff and R. Mandelbaum, arXiv:1702.02600 (2017), arXiv:1702.02600 [astro-ph.C].
[87] E. S. Sheldon and E. M. Huff, Astrophys. J. **841**, 24 (2017), arXiv:1702.02601 [astro-ph.CO].
[88] D. Coe, N. Benitez, S. F. Sanchez, M. Jee, R. Bouwens, and H. Ford, Astron. J. **132**, 926 (2006), arXiv:astro-ph/0605262 [astro-ph].
[89] J. Zuntz, E. Sheldon, *et al.* (DES), Mon. Not. Roy. Astron. Soc. **481**, 1149 (2018), arXiv:1708.01533 [astro-ph.CO].
[90] B. Hoyle, D. Gruen, *et al.* (DES), Mon. Not. Roy. Astron. Soc. **478**, 592 (2018), arXiv:1708.01532 [astro-ph.CO].
[91] J. Elvin-Poole *et al.* (DES), Phys. Rev. **D98**, 042006 (2018), arXiv:1708.01536 [astro-ph.CO].
[92] J. Prat, C. Sanchez, *et al.* (DES), Phys. Rev. **D98**, 042005 (2018), arXiv:1708.01537 [astro-ph.CO].
[93] M. A. Troxel *et al.* (DES), Phys. Rev. **D98**, 043528 (2018), arXiv:1708.01538 [astro-ph.CO].
[94] M. Jarvis, G. Bernstein, and B. Jain, Mon. Not. Roy. Astron. Soc. **352**, 338 (2004), arXiv:astro-ph/0307393 [astro-ph].
[95] E. Krause and T. Eifler, Mon. Not. Roy. Astron. Soc. **470**, 2100 (2017), arXiv:1601.05779 [astro-ph.CO].
[96] A. Cooray and R. K. Sheth, Phys. Rept. **372**, 1 (2002), arXiv:astro-ph/0206508 [astro-ph].
[97] M. A. Troxel *et al.* (DES), Mon. Not. Roy. Astron. Soc. **479**, 4998 (2018), arXiv:1804.10663 [astro-ph.CO].
[98] M. Crocce *et al.* (DES), Mon. Not. Roy. Astron. Soc. (2018).
[99] S. Avila *et al.* (DES), Mon. Not. Roy. Astron. Soc. **479**, 94 (2018), arXiv:1712.06232 [astro-ph.CO].
[100] A. J. Ross *et al.*, Mon. Not. Roy. Astron. Soc. **472**, 4456 (2017), arXiv:1705.05442 [astro-ph.CO].
[101] H. Camacho *et al.* (DES), Mon. Not. Roy. Astron. Soc. **487**, 3870 (2019), arXiv:1807.10163 [astro-ph.CO].
[102] K. C. Chan *et al.* (DES), Mon. Not. Roy. Astron. Soc. **480**, 3031 (2018), arXiv:1801.04390 [astro-ph.CO].
[103] D. A. Goldstein *et al.* (DES), Astron. J. **150**, 82 (2015), [Erratum: Astron. J.150,165(2015)], arXiv:1504.02936 [astro-ph.IM].
[104] R. Kessler *et al.* (DES), Astron. J. **150**, 172 (2015), arXiv:1507.05137 [astro-ph.IM].
[105] D. L. Burke *et al.* (DES), Astron. J. **155**, 41 (2017), arXiv:1706.01542 [astro-ph.IM].
[106] J. Lasker *et al.* (DES), Mon. Not. Roy. Astron. Soc. **485**, 5329 (2019), arXiv:1811.02380 [astro-ph.CO].
[107] D. Brout *et al.* (DES), Astrophys. J. **874**, 106 (2019), arXiv:1811.02378 [astro-ph.IM].
[108] M. Smith, C. B. D'Andrea, *et al.* (DES), The Astronomical Journal **160**, 267 (2020), arXiv:1811.09565 [astro-ph.CO].
[109] R. Kessler *et al.* (DES), Mon. Not. Roy. Astron. Soc. **485**, 1171 (2019), arXiv:1811.02379 [astro-ph.CO].
[110] D. Scolnic and R. Kessler, Astrophys. J. **822**, L35 (2016), arXiv:1603.01559 [astro-ph.CO].
[111] M. Hicken, W. M. Wood-Vasey, S. Blondin, P. Challis, S. Jha, P. L. Kelly, A. Rest, and R. P. Kirshner, Astrophys. J. **700**, 1097 (2009), arXiv:0901.4804 [astro-ph.CO].
[112] M. Hicken *et al.*, Astrophys. J. Suppl. **200**, 12 (2012), arXiv:1205.4493 [astro-ph.CO].
[113] C. Contreras *et al.*, Astron. J. **139**, 519 (2010), arXiv:0910.3330 [astro-ph.CO].
[114] F.-S. Kitaura *et al.*, Mon. Not. Roy. Astron. Soc. **456**, 4156 (2016), arXiv:1509.06400 [astro-ph.CO].
[115] A. G. Sanchez *et al.* (BOSS), Mon. Not. Roy. Astron. Soc. **464**, 1493 (2017), arXiv:1607.03146 [astro-ph.CO].
[116] J. Zuntz, M. Paterno, E. Jennings, D. Rudd, A. Manzotti, S. Dodelson, S. Bridle, S. Sehrish, and J. Kowalkowski, Astron. Comput. **12**, 45 (2015), arXiv:1409.3409 [astro-ph.CO].
[117] F. Feroz and M. P. Hobson, Mon. Not. Roy. Astron. Soc. **384**, 449 (2008), arXiv:0704.3704 [astro-ph].
[118] F. Feroz, M. P. Hobson, and M. Bridges, Mon. Not. Roy. Astron. Soc. **398**, 1601 (2009), arXiv:0809.3437 [astro-

ph].
[119] F. Feroz, M. Hobson, E. Cameron, and A. Pettitt, Open J. Astrophys. **2**, 10 (2019), arXiv:1306.2144 [astro-ph.IM].
[120] W. J. Handley, M. P. Hobson, and A. N. Lasenby, Mon. Not. Roy. Astron. Soc. **450**, L61 (2015), arXiv:1502.01856 [astro-ph.CO].
[121] A. Lewis, "GetDist: MCMC sample analysis, plotting and GUI," (2019).
[122] P. Lemos, F. Köhlinger, W. Handley, B. Joachimi, L. Whiteway, and O. Lahav, Mon. Not. Roy. Astron. Soc. **496**, 4647 (2020), arXiv:1910.07820 [astro-ph.CO].
[123] W. Handley, J. Open Source Softw. **4**, 1414 (2019), arXiv:1905.04768 [astro-ph.IM].
[124] M. Raveri and W. Hu, Phys. Rev. D **99**, 043506 (2019), arXiv:1806.04649 [astro-ph.CO].
[125] W. Handley and P. Lemos, Phys. Rev. D **100**, 023512 (2019), arXiv:1903.06682 [astro-ph.CO].
[126] F. Beutler *et al.* (BOSS), Mon. Not. Roy. Astron. Soc. **444**, 3501 (2014), arXiv:1403.4599 [astro-ph.CO].
[127] I. G. Mccarthy, S. Bird, J. Schaye, J. Harnois-Deraps, A. S. Font, and L. Van Waerbeke, Mon. Not. Roy. Astron. Soc. **476**, 2999 (2018), arXiv:1712.02411 [astro-ph.CO].
[128] V. Poulin, K. K. Boddy, S. Bird, and M. Kamionkowski, Phys. Rev. D **97**, 123504 (2018), arXiv:1803.02474 [astro-ph.CO].
[129] Y. Dirian, Phys. Rev. D **96**, 083513 (2017), arXiv:1704.04075 [astro-ph.CO].
[130] S. Samuroff *et al.* (DES), Mon. Not. Roy. Astron. Soc. **489**, 5453 (2019), arXiv:1811.06989 [astro-ph.CO].
[131] Dark Energy Survey Collaboration (DES, SPT), Phys. Rev. D **100**, 023541 (2019), arXiv:1810.02322 [astro-ph.CO].
[132] K. Aylor, M. Joy, L. Knox, M. Millea, S. Raghunathan, and W. K. Wu, Astrophys. J. **874**, 4 (2019), arXiv:1811.00537 [astro-ph.CO].
[133] J. L. Bernal, L. Verde, and A. G. Riess, JCAP **1610**, 019 (2016), arXiv:1607.05617 [astro-ph.CO].
[134] K. L. Pandey, T. Karwal, and S. Das, JCAP **07**, 026 (2020), arXiv:1902.10636 [astro-ph.CO].
[135] T. Tröster *et al.*, Astron. Astrophys. **633**, L10 (2020), arXiv:1909.11006 [astro-ph.CO].
[136] G. D'Amico, J. Gleyzes, N. Kokron, K. Markovic, L. Senatore, P. Zhang, F. Beutler, and H. Gil-Marín, JCAP **05**, 005 (2020), arXiv:1909.05271 [astro-ph.CO].
[137] M. M. Ivanov, M. Simonović, and M. Zaldarriaga, Phys. Rev. D **101**, 083504 (2020), arXiv:1912.08208 [astro-ph.CO].
[138] C.-H. To *et al.* (Dark Energy Survey), arXiv:2008.10757 (2020), arXiv:2008.10757 [astro-ph.CO].
[139] E. J. Baxter *et al.* (DES), Phys. Rev. **D99**, 023508 (2019), arXiv:1802.05257 [astro-ph.CO].
[140] E. Jones, T. Oliphant, P. Peterson, *et al.*, "SciPy: Open source scientific tools for Python," (2001–), [Online; accessed 2019].
[141] T. E. Oliphant, *A guide to NumPy* (Trelgol Publishing, USA, 2006).
[142] J. D. Hunter, Computing in Science & Engineering **9**, 90 (2007).
[143] J. Schaye, C. Dalla Vecchia, C. M. Booth, R. P. C. Wiersma, T. Theuns, M. R. Haas, S. Bertone, A. R. Duffy, I. G. McCarthy, and F. van de Voort, Mon. Not. Roy. Astron. Soc. **402**, 1536 (2010), arXiv:0909.5196 [astro-ph.CO].
[144] J. A. Blazek, N. MacCrann, M. A. Troxel, and X. Fang, Phys. Rev. **D100**, 103506 (2019), arXiv:1708.09247 [astro-ph.CO].
[145] N. Padmanabhan *et al.* (SDSS), Mon. Not. Roy. Astron. Soc. **378**, 852 (2007), arXiv:astro-ph/0605302 [astro-ph].
[146] G. M. Bernstein, Astrophys. J. **695**, 652 (2009), arXiv:0808.3400 [astro-ph].
[147] P. McDonald and A. Roy, JCAP **08**, 020 (2009), arXiv:0902.0991 [astro-ph.CO].
[148] T. Baldauf, U. Seljak, V. Desjacques, and P. McDonald, Phys. Rev. D **86**, 083540 (2012), arXiv:1201.4827 [astro-ph.CO].
[149] J. E. McEwen, X. Fang, C. M. Hirata, and J. A. Blazek, JCAP **09**, 015 (2016), arXiv:1603.04826 [astro-ph.CO].
[150] J. DeRose *et al.* (DES), arXiv:1901.02401 (2019), arXiv:1901.02401 [astro-ph.CO].